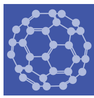 *nanomaterials*

MDPI

Review

Progress in Advanced Infrared Optoelectronic Sensors

Xiang Yu [1,2,3], Yun Ji [4,*], Xinyi Shen [1,2,3] and Xiaoyun Le [1,2,3,*]

1 School of Physics, Beihang University, Beijing 100191, China
2 Beijing Advanced Innovation Center for Big Data-Based Precision Medicine, School of Medicine and Engineering, Beihang University, Beijing 100191, China
3 Beijing Key Laboratory of Advanced Nuclear Energy Materials and Physics, Beihang University, Beijing 100191, China
4 Department of Electrical and Computer Engineering, National University of Singapore, 4 Engineering Drive 3, Singapore 117583, Singapore
* Correspondence: jiyun@nus.edu.sg (Y.J.); xyle@buaa.edu.cn (X.L.)

Abstract: Infrared optoelectronic sensors have attracted considerable research interest over the past few decades due to their wide-ranging applications in military, healthcare, environmental monitoring, industrial inspection, and human–computer interaction systems. A comprehensive understanding of infrared optoelectronic sensors is of great importance for achieving their future optimization. This paper comprehensively reviews the recent advancements in infrared optoelectronic sensors. Firstly, their working mechanisms are elucidated. Then, the key metrics for evaluating an infrared optoelectronic sensor are introduced. Subsequently, an overview of promising materials and nanostructures for high-performance infrared optoelectronic sensors, along with the performances of state-of-the-art devices, is presented. Finally, the challenges facing infrared optoelectronic sensors are posed, and some perspectives for the optimization of infrared optoelectronic sensors are discussed, thereby paving the way for the development of future infrared optoelectronic sensors.

Keywords: infrared optoelectronic sensor; photovoltaic effect; responsivity; 2D materials; image sensing

Citation: Yu, X.; Ji, Y.; Shen, X.; Le, X. Progress in Advanced Infrared Optoelectronic Sensors. *Nanomaterials* **2024**, *14*, 845. https://doi.org/10.3390/nano14100845

Academic Editor: Mircea Dragoman

Received: 8 April 2024
Revised: 9 May 2024
Accepted: 10 May 2024
Published: 12 May 2024

Copyright: © 2024 by the authors. Licensee MDPI, Basel, Switzerland. This article is an open access article distributed under the terms and conditions of the Creative Commons Attribution (CC BY) license (https://creativecommons.org/licenses/by/4.0/).

1. Introduction

The infrared region of the electromagnetic spectrum, spanning near-infrared regime (0.78–2.5 μm), mid-infrared regime (2.5–25 μm), and far-infrared regime (25–1000 μm), is of significant interest due to its wide applications in optical communication, health monitoring, industrial inspection, environment monitoring, and human–computer interaction systems [1]. Infrared optoelectronic sensors, which are able to selectively convert infrared photons into electrical signals, play a crucial role in advancing the utilization of infrared light [2,3]. According to their energy conversion processes, infrared optoelectronic sensors can be broadly classified into photon-type, photothermal-type, and hybrid-type devices. Photon-type optoelectronic sensors utilize photosensitive semiconductors to absorb incident infrared photons, exciting bound-state electrons to the conduction band of the photosensitive semiconductor to generate photogenerated electron–hole pairs. These electron–hole pairs are then separated and transported under external or built-in electric fields to form electrical signals, achieving a direct conversion of light energy to electricity. In contrast, photothermal-type infrared optoelectronic sensors first absorb infrared photons to generate thermal energy through the photothermal effect. Then, that thermal energy induces temporal or spatial variations in the temperature of the sensors, driving carrier migration for electrical signal generation, thereby enabling indirect conversion of the light energy to electricity. Hybrid-type infrared optoelectronic sensors leverage infrared photons to simultaneously generate electron–hole pairs and induce temperature variations for measurable electrical signals. Commercialized infrared optoelectronic sensors primarily rely on epitaxially grown crystalline inorganic III–V compound semiconductors [4], which are insufficient to meet the ever-changing demands of various applications. Hence, a variety

of photosensitive materials and nanostructures have been developed to construct diverse infrared optoelectronic sensors. These photosensitive materials and nanostructures include narrow-bandgap two-dimensional (2D) semiconductor materials with high carrier mobility and absorption coefficients [5,6], a narrow-bandgap conjugated polymer [7,8], ferroelectric materials with high pyroelectric coefficients [9,10], and homo-/heterojunction structures with a strong built-in electrical field for carrier separation and transport [11–14]. With diverse functional materials and device configurations, the performance metrics of infrared optoelectronic sensors, including their response range, responsivity, detectivity, and response speed, can vary significantly, tailoring them to specific demands. The rapid development of infrared optoelectronic sensors, together with the daily evolution and industrial requirements of infrared applications, highlights the critical need for a comprehensive understanding of these sensors.

This paper provides a comprehensive review of recent advancements in infrared optoelectronic sensors. It begins by elucidating their working mechanisms, followed by an introduction to the key metrics utilized to evaluate device performance. Next, it offers an overview of promising materials and nanostructures for high-performance infrared optoelectronic sensors, along with the room-temperature performance of state-of-the-art devices. Moreover, it outlines the recent applications of infrared optoelectronic sensors. Finally, it discusses the challenges and prospects facing infrared optoelectronic sensors, providing guidance for the development of future infrared optoelectronic sensors.

2. Working Mechanisms

2.1. Photovoltaic Effect

The photovoltaic effect refers to the phenomenon by which photoexcited electron–hole pairs are generated, separated, and transported under the driving force of internal electric fields to produce electric signals [15]. Based on the photovoltaic effect, infrared optoelectronic sensors absorb light to generate electron–hole pairs, which are then extracted and accelerated by internal electric fields, resulting in sizable photocurrent/photovoltaic signals. Their internal electric fields mainly arise from the formation of a depletion region at the interface of Schottky junctions [16,17], semiconducting homojunctions/heterojunctions [18–21], and semiconductor/electrolyte junctions [22,23].

The energy difference between the Fermi levels of metals and semiconductors causes a large potential difference, forming Schottky barrier junctions at metal/semiconductor interfaces. The mechanism of electrical signal generation in Schottky junctions can be understood with the assistance of energy band diagrams. Figure 1a illustrates the energy band diagram of a typical Schottky junction formed at a Au/InSe interface [24]. Due to the Fermi level difference between Au and InSe, electrons in the InSe migrate toward the Au electrode, leaving behind positively charged ions on the InSe side. Consequently, the energy bands of the InSe are bent upward to form a Schottky junction at the Au/InSe interface. Upon illumination, photoexcited electron–hole pairs can be separated and extracted by the Schottky junction, generating electrical signals.

A p-n junction is formed due to the diffusion of carriers under the driving force of the carrier concentration difference in p-type and n-type semiconductors. For example, when p-type black phosphorous (BP) and n-type $PdSe_2$ come into contact, the holes in BP and electrons in $PdSe_2$ diffuse in opposite directions, establishing a built-in electric field at the p-BP/n-$PdSe_2$ interface, as shown in Figure 1b [25]. Upon illumination, electrons in the valence band of BP can be excited to the conduction band, generating photogenerated electron–hole pairs. Subsequently, photogenerated electron–hole pairs near the BP/$PdSe_2$ interface can diffuse to the p-n junction, where they are separated and swept toward opposite directions by the built-in electric field, forming electrical signals in the external circuit. Infrared optoelectronic sensors based on p-n junctions can generate photogenerated electron–hole pairs based on two main approaches: the band-to-band transition of electrons within an individual semiconductor (Figure 1b), and the interlayer transition of electrons at the interface of type-II staggered semiconductors. Figure 1c presents a representative

energy band diagram of interlayer electron transition based on a type-II $MoTe_2/MoS_2$ heterostructure [26]. Under illumination, the electrons in the valence band of the $MoTe_2$ can be excited to the conduction band of the MoS_2, thereby creating electrical signals. Due to the small energy offset (0.657 eV) between the valence band of the $MoTe_2$ and the conduction band of the MoS_2, an infrared response is beyond the limits of the intrinsic bandgaps of the MoS_2 and $MoTe_2$ materials.

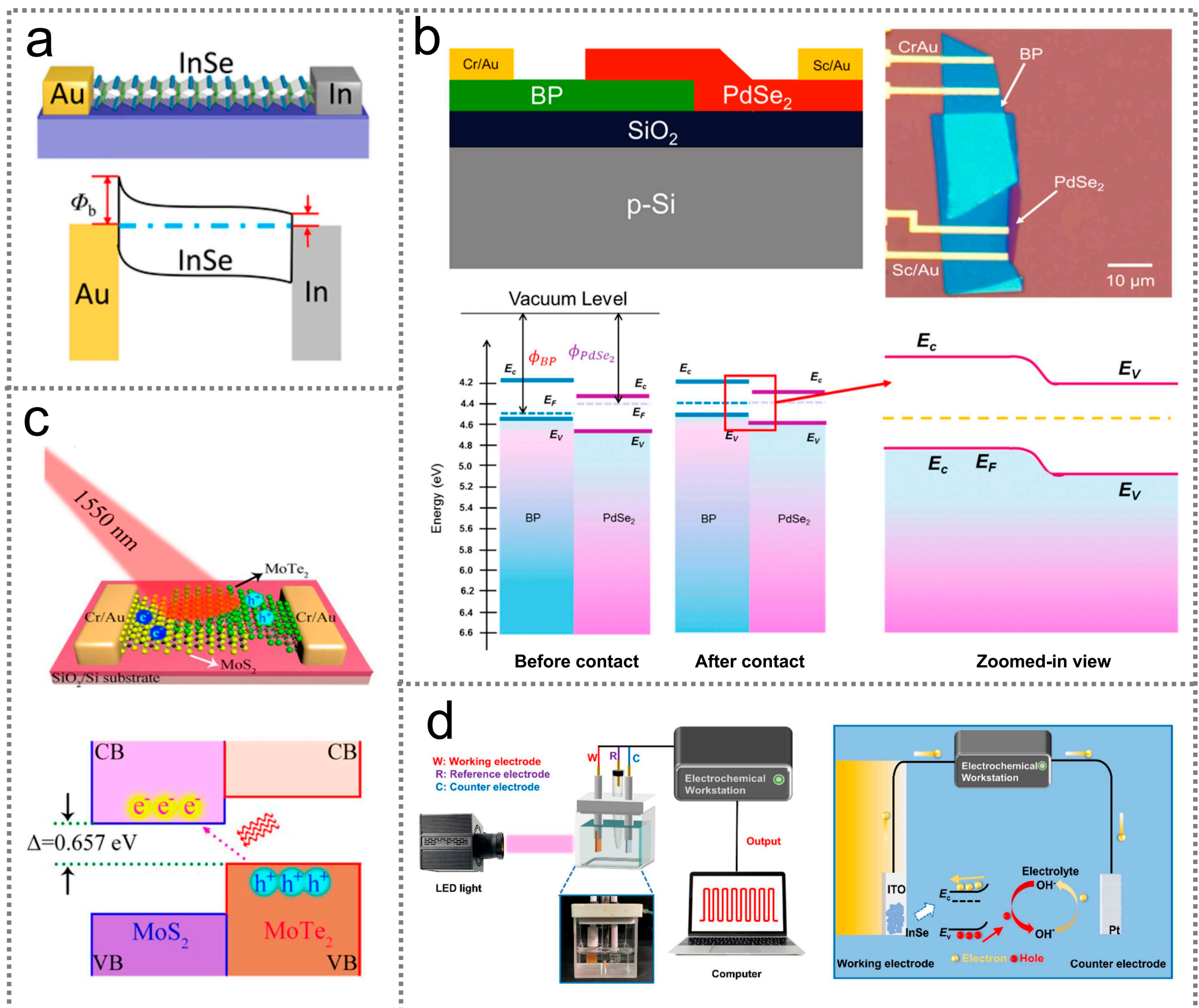

Figure 1. Working mechanisms of photon-type infrared optoelectronic sensors. (**a**) Working mechanism of an infrared optoelectronic sensor based on Schottky junctions [24] (with permission from the American Chemical Society, 2018). (**b**) Working mechanism of an infrared optoelectronic sensor based on a p-n junction with intralayer transition [25] (with permission from the American Chemical Society, 2020). (**c**) Working mechanism of an infrared optoelectronic sensor based on a p-n junction with interlayer transition [26] (with permission from the American Chemical Society, 2016). (**d**) Working mechanism of an infrared optoelectronic sensor based on a semiconductor/electrolyte junction [23] (with permission from the American Chemical Society, 2022).

A semiconductor/electrolyte junction is established because of the disparity between the work functions of semiconductors and redox potential electrolytes. Figure 1d displays the working mechanism of a representative infrared optoelectronic sensor based on a semiconductor/electrolyte junction, where InSe is contact with the electrolyte [23]. Since the work function of InSe is smaller than the redox potential of the electrolyte, electrons in the InSe flow into the electrolyte until an electronic equilibrium is achieved. As a consequence, a built-in electric field is established and works similar to a Schottky junction. Upon illumination, the photogenerated electron–hole pairs generated in the InSe are separated and transferred under the driving force of the built-in electric field, with electrons and holes moving toward the Pt and ITO electrodes, respectively. Therefore, light-induced electrical signals are created in the external circuit.

2.2. Photoconductive Effect

The photoconductive effect is an effect that means the conductivity of semiconductors changes with the incident light's intensity. The generation of an electric signal in infrared optoelectronic sensors based on the photoconductive effect is quite similar to that based on the photovoltaic effect, wherein photogenerated electron–hole pairs are created by absorbing photons. However, in photoconductive sensors, the separation and transport of photogenerated electron–hole pairs require an external electric field as the driving force [27,28].

2.3. Pyroelectric Effect

The pyroelectric effect refers to the phenomenon in which electric charges are generated in response to a change in spontaneous polarization caused by a temperature variation, which typically occurs in certain polar materials [29]. Pyroelectric infrared optoelectronic sensors have several advantages over other types of sensors, such as room-temperature operation, a wide wavelength response, and low cost, enabling their use for various applications [30–32]. To elucidate the working mechanism of pyroelectric infrared optoelectronic sensors, the process of electrical signal generation in a device utilizing a ferroelectric PMN-PT layer as its pyroelectric component is introduced. Figure 2a exhibits the schematic diagram and output current of a PMN-PT pyroelectric infrared optoelectronic sensor, where the PMN-PT layer is sandwiched between the top Ag nanowire electrode and the bottom Au electrode [33]. Under dark conditions ($\mathrm{d}T/\mathrm{d}t = 0$), the electric dipoles within the PMN-PT layer are well aligned and oscillate around their aligned axes to a certain degree, resulting in a stable spontaneous polarization strength. As a consequence, negative and positive charges are attracted to the Ag nanowire electrode and the Au electrode, respectively, reaching an equilibrium state at which no current can be detected in the external circuit. Upon illumination, the temperature of the PMN-PT sensor increases due to photothermal effect ($\mathrm{d}T/\mathrm{d}t > 0$), intensifying the oscillation of the electric dipoles and reducing the spontaneous polarization strength in the PMN-PT. Hence, the attracted negative and positive charges move toward the Au electrode and the Ag nanowire electrode, respectively, until a new thermal equilibrium state is established. Consequently, a negative current signal is observed in the external circuit. When the light is removed, the temperature of the sensor gradually decreases to its original state ($\mathrm{d}T/\mathrm{d}t < 0$), which suppresses the oscillation of electric dipoles in the PMN-PT, leading to a higher average spontaneous polarization strength. Consequently, a positive current signal is generated in the external circuit. This light-induced pyroelectric current can be obtained using the following equation [34]:

$$I_{\mathrm{pyro}} = \frac{\eta p_{C} S P}{c d A} \quad (1)$$

where η stands for the emissivity of the illuminated device surface, P is the incident light's intensity, d is the device thickness, P_{c} represents the pyroelectric coefficient, c stands for the specific heat capacity, and A is a parameter related to the device's thermal time constant. For years, the pyroelectric effect has been considered to only exist in non-centrosymmetric

materials, and always exhibited a sharp decay away from the phase transition temperature, thereby limiting its working temperature. In 2020, the pyroelectric effect was demonstrated in interfaces with polar symmetry, which exhibit a weak temperature dependence, suitable for utilization across a wide temperature range [35].

2.4. Photothermoelectric Effect

The photothermoelectric effect leverages the coupling of the photothermal effect and thermoelectric effect in semiconductors to generate electric potential [36]. Figure 2b shows a typical photothermoelectric infrared optoelectronic sensor which possesses a planar device configuration with electrodes positioned at both ends of a semiconductor [37]. When localized illumination is applied to the sensor, a temperature gradient ΔT within the semiconductor is established due to the nonuniform heating caused by the incident light. The temperature gradient ΔT drives charge carriers to diffuse from the hotter side to the colder side of the semiconductor. Consequently, an electric potential difference ΔV is produced owing to the Seebeck effect. The relationship between the electric potential difference ΔV and the temperature gradient ΔT can be expressed utilizing the following formula [38]:

$$\Delta V = S\Delta T \tag{2}$$

where S represents the Seebeck coefficient of the semiconductor. The Seebeck coefficient can be described by the Mott equation [39]:

$$S = -\frac{\pi^2 k_B^2 T}{3e}\left(\frac{\mathrm{d}(\ln\sigma)}{\mathrm{d}E}\right)\Big|_{E=E_\mathrm{f}} \tag{3}$$

where k_B stands for the Boltzmann constant, T represents the absolute temperature, e is the elementary charge, σ is the electrical conductivity, and E_f stands for the Fermi level. According to this equation, semiconductor materials with high electrical conductivity, a high light absorption coefficient, low thermal conductivity, and a low heat capacity can contribute to high-performance photoelectric infrared optoelectronic sensors.

Besides n-type or p-type semiconductors, photothermoelectric infrared optoelectronic sensors can also be constructed by utilizing the p-n junctions in certain materials. As illustrated in Figure 2c, a p-n homojunction in a BP material can be achieved based on electrical doping [40]. Under illumination, the electrons and holes in the homojunction are driven by the temperature gradient and transported toward opposite directions, resulting in enhanced current signals on both sides. Since the fundamental driving force for charge carrier diffusion is the temperature gradient-induced carrier concentration gradient, highly sensitive thermoelectric infrared optoelectronic sensors can be realized with device configurations that allow for larger temperature gradients.

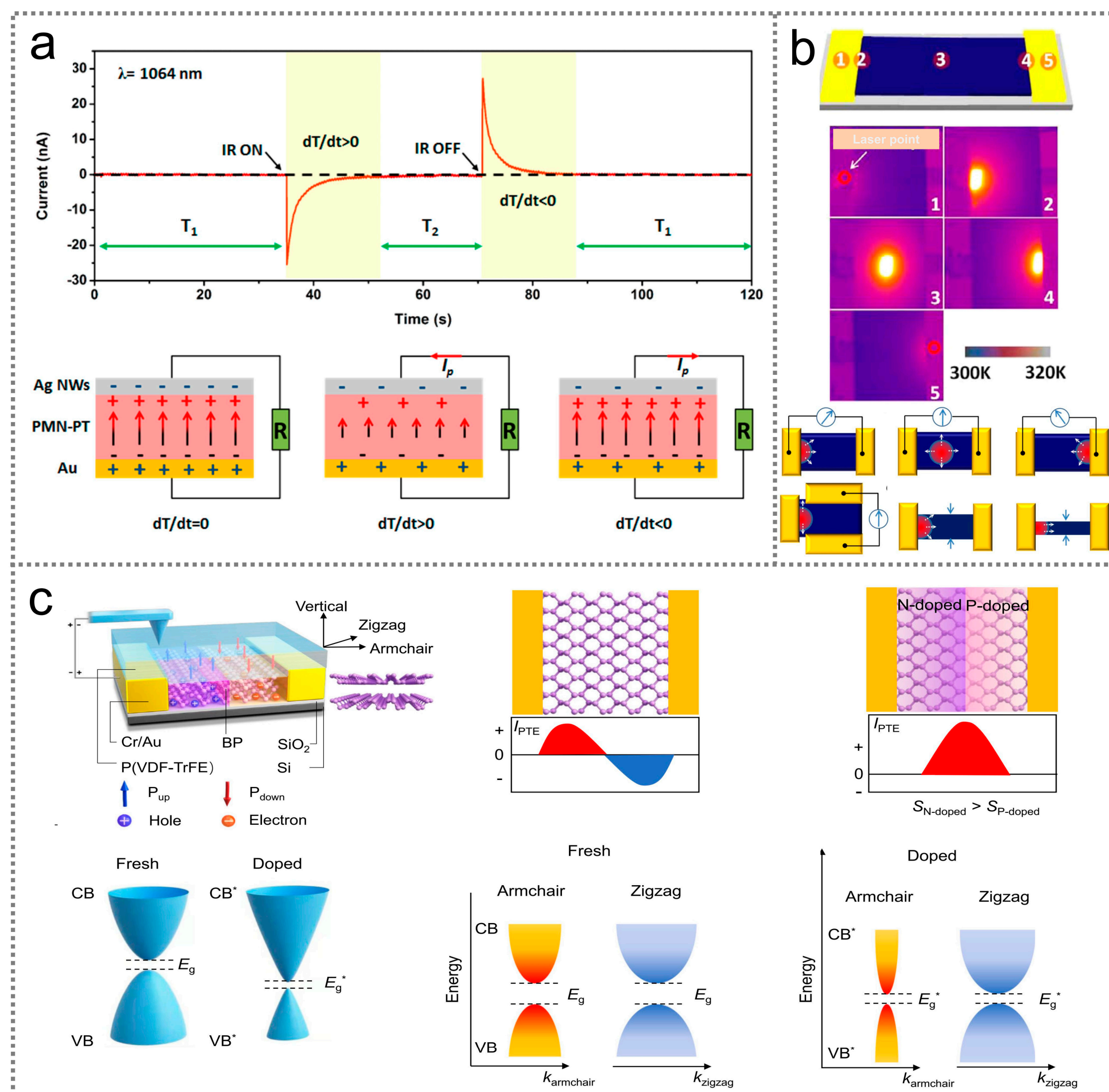

Figure 2. Working mechanism of photothermal-type infrared optoelectronic sensors. (**a**) Working mechanism of an infrared optoelectronic sensor based on the pyroelectric effect [33] (with permission from the American Chemical Society, 2016). (**b**) Working mechanism of an infrared optoelectronic sensor on the basis of the photothermoelectric effect in a single semiconductor [37] (with permission from the American Chemical Society, 2015). (**c**) Working mechanism of an infrared optoelectronic sensor based on the photothermoelectric effect in a p-n semiconducting homojunction. CB, VB, and *Eg* stand for the conduction band, valence band and bandgap of pristine BP, respectively. CB*, VB*, and *Eg** are the conduction band, valence band, and bandgap of doped BP [40] (with permission from Springer Nature, 2022).

2.5. Others

Taking the advantages of photovoltaic and photothermal effects, infrared optoelectronic sensors can be constructed based on the pyroelectric–photovoltaic effect, which is a coupling of pyroelectric polarization, semiconductor/ferroelectrics characteristics, and photoexcitation processes [41]. Figure 3a illustrates the working mechanism of a pyroelectric–photovoltaic infrared optoelectronic sensor, which is constructed based on a p-Si/n-Ag_2Se heterojunction [42]. Upon light illumination, photogenerated electrons and holes move toward the Ag_2Se and Si sides due to the photovoltaic effect, respectively. As a result, a positive electric signal is produced in the external circuit. Meanwhile, a rapid transient increase in the temperature is achieved in the Ag_2Se because of the photothermal effect, leading to a positive pyroelectric signal traversing the Ag_2Se. Since the light-induced

photovoltaic signal and pyroelectric signal possess the same polarity, the electrical signal of a pyroelectric–photovoltaic infrared optoelectronic sensor can achieve enhanced infrared responses compared to infrared optoelectronic sensors based on the pyroelectric effect or photovoltaic effect alone.

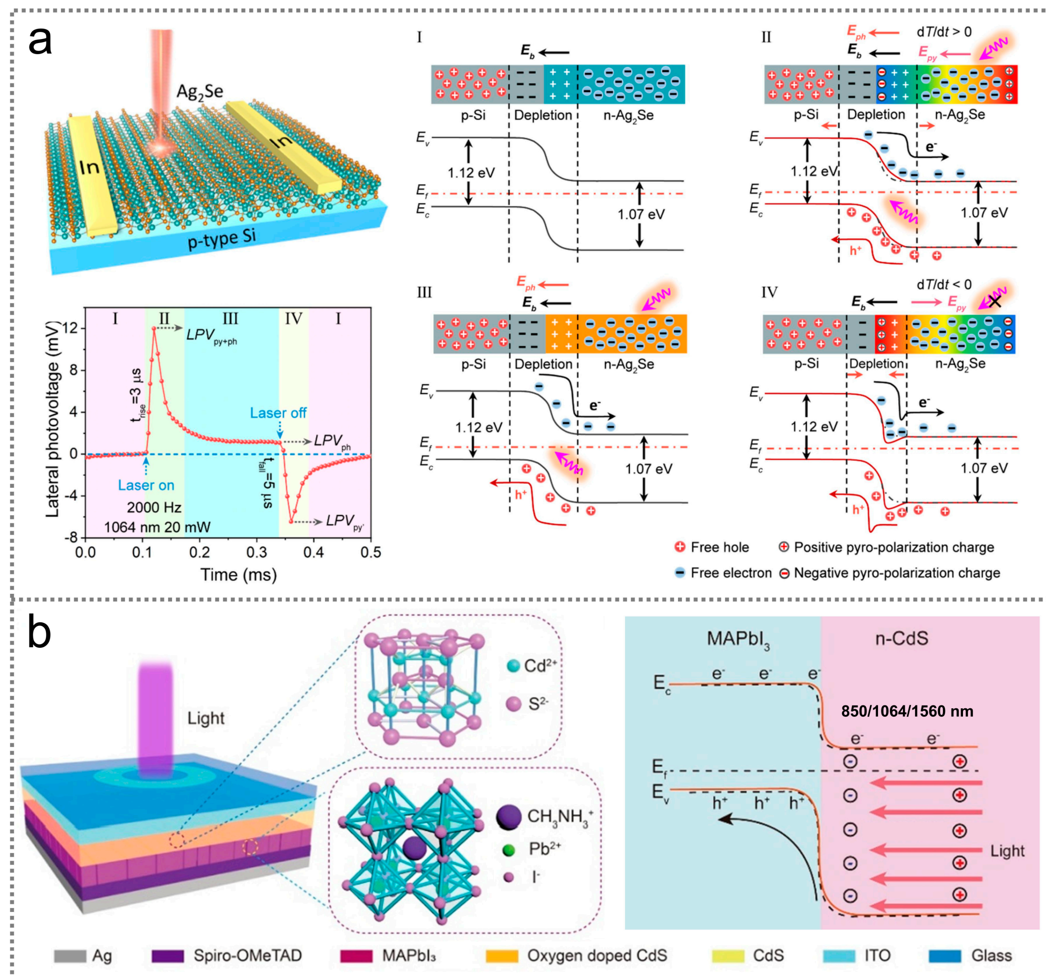

Figure 3. The working mechanism of infrared optoelectronic sensors based on coupling effects. (**a**) Working mechanism of an infrared optoelectronic sensor based on the pyroelectric–photovoltaic effect [42] (with permission from the American Chemical Society, 2022). (**b**) Working mechanism of an infrared optoelectronic sensor based on the pyroelectric–photothermoelectric effect [43] (with permission from the American Chemical Society, 2023).

The pyroelectric–photothermoelectric effect is another vital mechanism for constructing infrared optoelectronic sensors because it maximizes the light-induced heat to generate electrical signals. Figure 3b illustrates the working mechanism of a pyroelectric–photothermoelectric infrared optoelectronic sensor, where a heterostructure composed of $CH_3NH_3PbI_3$ ($MAPbI_3$) and CdS materials serves as the photosensitive component [43]. Under illumination, the temperature of the sensor gradually increases due to the photothermal effect, leading to temporal variations in the device temperature for pyroelectric signals. Moreover, the photothermal effect can create a longitudinal temperature gradient in the $MAPbI_3$/CdS heterojunction, thereby resulting in photothermoelectric signals that align with the pyroelectric signals. The combination of the pyroelectric and photothermoelectric effects is promising for achieving high responsivity.

3. Key Performance Metrics

The critical parameters for evaluating the performance of infrared optoelectronic sensors include their spectral response range, responsivity R, response speed, gain G, Noise-equivalent power NEP, specific detectivity D^*, on/off ratio R_{ratio}, linear dynamic range LER, and external quantum efficiency EQE.

The spectral response range refers to the region of wavelength that the infrared optoelectronic sensors can detect. Each infrared optoelectronic sensor can only respond to a specific wavelength due to the limitations imposed by their photosensitive material's properties, working mechanisms, and device configurations.

Responsivity R is one the most important device parameters for infrared optoelectronic sensors, as it represents the magnitude of the photocurrent produced by illumination at a given light intensity and wavelength. Responsivity R can be defined as

$$R = \frac{I_{ph}}{P_{in}} \quad (4)$$

where I_{ph} is the light-induced current density (A cm^{-2}) of the infrared optoelectronic sensor and P_{in} stands for the incident light power density (W cm^{-2}).

Response speed can be evaluated by the response time and recovery time. Generally, the response time and recovery time are defined as the time required for the photocurrent/photovoltage to increase from 10% to 90% and to decrease from 90% to 10%, respectively. The response speed relies on many factors, especially material properties, interface defects, and temperature.

Gain G reflects the magnitude of recycled photoexcitation based on the accumulation mechanism, which is determined by the lifetime of excitons. Gain G can be expressed using the formula

$$G = \frac{\tau_{life}}{\tau_{transit}} = \frac{\tau_{life}}{L^2/\mu V} \quad (5)$$

where τ_{life} stands for the lifetime of photogenerated excitons and $\tau_{transit}$ means the time taken for photogenerated excitons to transit through a channel. L represents the channel length, μ is the carrier mobility, and V is the voltage exerted on the channel. In a photovoltaic optoelectronic infrared sensor, the gain is equal to 1 unless carrier multiplication effects are involved. However, in a photoconductive optoelectronic infrared sensor, one type of carrier (typically holes) is captured in trap states, while the other type of carrier (electrons) traverses the channel. If the lifetime τ_{life} of the holes is larger than the transit time $\tau_{transit}$ of the electrons, the electrons can recirculate many times before recombining with the captured holes, resulting in a gain greater than 1. In this case, increasing the trapping of holes can lead to a higher gain [44,45].

Noise-equivalent power (NEP) is the minimum light power required to distinguish a signal from noise in an optoelectronic sensor. The NEP can be utilized to evaluate the sensitivity of the device and is defined using the equation

$$\text{NEP} = \left(\frac{I_n}{\Delta f^{1/2} R}\right) \quad (6)$$

where I_n stands for the noise current detected in dark conditions and Δf represents the electrical bandwidth of the noise measurement.

The specific detectivity D^* reflects the sensitivity of the optoelectronic sensors to weak light detection and is given by the following formula:

$$D^* = \frac{A^{1/2} R}{\text{NEP}} = \frac{R(A\Delta f)^{1/2}}{I_n} \quad (7)$$

where A is the effective device area. The unit of specific detectivity D^* is Jones (1 Jones = 1 cm Hz$^{1/2}$ W^{-1}).

The on/off ratio R_{ratio} is the ratio between the dark noise current and the photocurrent and can be calculated by the formula

$$R_{\text{ratio}} = \frac{I_{\text{ph}}}{I_{\text{n}}} \quad (8)$$

The linear dynamic range LDR is the specific range in which the photocurrent shows a linear relationship to the incident light power. The linear dynamic range LDR is described by the following equation:

$$\text{LDR} = 20\log\left(\frac{P_{\text{max}}}{P_{\text{min}}}\right) = 20\log\left(\frac{J_{\text{max}}}{J_{\text{min}}}\right) \quad (9)$$

where P_{max} stands for the maximum incident light power beyond which the photoresponses deviate from their linear region and P_{min} represents the minimum detectable light density. J_{max} and J_{min} are the maximum and minimum values of photocurrent density, respectively.

The external quantum efficiency EQE depends on the number of primary charge carriers generated per single input photon, which plays an important role in determining responsivity. External quantum efficiency EQE can be calculated using the formula

$$\text{EQE} = \frac{I_{\text{ph}}h\nu}{P_{\text{in}}e} \quad (10)$$

where $h\nu$ represents the photon's energy.

4. Materials and Their Performances

4.1. 2D Semimetals and Semiconductors

Two-dimensional materials hold great potential for building highly integrated and efficient infrared optoelectronic sensors due to their thickness-tunable bandgaps, high carrier mobility, and strong optical absorption. Because their infrared range corresponds to a low photon energy of about 1.55 eV, most of the 2D materials used in infrared optoelectronic sensing devices are semimetals and narrow-bandgap semiconductors. Semimetals, such as graphene, TaAs, $PdTe_2$, WTe_2, and TaIrTe [46–48], possess gapless electronic band structures with linear cones, enabling broadband infrared sensing extending to the far-infrared spectral region [49]. The lifetime of the photogenerated carriers in semimetals is dramatically decreased via fast electron–electron scattering, thereby allowing for rapid responses [50]. However, because of their gapless nature, infrared optoelectronic sensors based on semimetals usually suffer from high dark currents. Narrow-bandgap 2D semiconductors, including BP [51], black AsP (B-AsP) [52], Bi_2O_2Se [53], tellurene [54], metal chalcogenides, and transition-metal dichalcogenides [55], exhibit thickness-tunable bandgaps, which contribute to their low dark currents. Table 1 summarizes the bandgaps of promising 2D materials for infrared sensing. Among these 2D materials, graphene, BP, and metal chalcogenides are most frequently utilized to fabricate infrared optoelectronic sensors.

Graphene, first mechanically exfoliated from graphite in 2004 [56], has become popular due to its intriguing electronic and optical properties. Graphene possesses an in-plane chemical bond connecting its carbon atoms and stacks through the van der Waals forces between its layers. In graphene, a single layer of carbon atoms with sp^2 hybridization arranged in a honeycomb lattice, with each carbon atom in-plane bonded to its three nearest carbon atoms, as illustrated in Figure 4a [57]. Graphene is gapless and dispersed linearly near the Dirac point, making it theoretically capable of responding to all photons. This property offers advantages for wideband photodetection, spanning from the ultraviolet to the terahertz spectral regimes [58]. The conductivity and mobility of graphene are mainly determined by its defects and are nearly independent of temperature [59]. With high carrier mobility (up to 2×10^5 $\text{cm}^2\ \text{V}^{-1}\ \text{s}^{-1}$) at room temperature [60], graphene enables ultrafast infrared sensing based on photovoltaic, photothermoelectric, and photoconductive effects.

BP is a direct-bandgap semiconductor with a thickness-tunable bandgap ranging from 0.3 eV to 2.0 eV. Since its rediscovery in 2014, BP has emerged as a preferred candidate for infrared optoelectronic sensing due to its unique characteristics, including its strong intralayer anisotropy, high mobility (10^3 cm^2 V^{-1} s^{-1}), and strong optical absorption [61–63]. Bulk BP possesses an orthorhombic structure with a $D_{2h}{}^{18}$ space group symmetry. Within a single atomic layer of BP, each phosphorous atom bonds with three neighboring atoms, resulting in two distinct directions: the armchair direction along its x axis, and the zigzag direction along its y axis, as illustrated in Figure 4b [64]. The highly anisotropic arrangement of phosphorous atoms results in anisotropic electric band dispersion, thereby leading to anisotropic optoelectronic properties. Benefiting from its moderate bandgap, large tunability, and anisotropy, few-layer BP holds significant promise for polarized infrared optoelectronic sensors. Due to its noncentrosymmetric structure, BP is expected to exhibit pyroelectricity. In addition, the bandgap of BP demonstrates anomalous strain dependence because of its puckered lattice structure, enabling the continuous and reversible tuning of its operating wavelengths during infrared optoelectronic sensing through strain modulation. With its combination of a narrow bandgap, high charge carrier concentration, and noncentrosymmetric structure, BP enables infrared optoelectronic sensing based on photovoltaic, photothermoelectric, and pyroelectric effects [65].

Non-transition metal chalcogenides with narrow and tunable bandgaps are emerging as popular candidates for the construction of infrared optoelectronic sensors. These materials possess chemical formulas of MX, MX_2, or M_2X_3, where M can be In, Ge, Bi, Sb, Pt, or Sn, and X can be S, Se, or Te. Among the non-transition metal chalcogenides, In-based narrow-bandgap materials such as InSe, α-In_2Se_3, and β-In_2Se_3 are notable. InSe exhibits a direct bandgap of 1.26 eV in bulk, and an indirect bandgap of 2.72 eV in monolayer [66]. Due to its small electron effective mass, InSe has a high electron mobility of about 10^3 cm^2 V^{-1} S^{-1} and a low electron–hole recombination rate, enabling a high optoelectronic response. Surface doping using $AuCl_3$ can modify the energy band structure of InSe, which facilitates the separation of photogenerated electron–hole pairs, leading to an improved optoelectronic sensing performance [67]. Two-dimensional α-In_2Se_3 with a noncentrosymmetric crystal structure exhibits robust ferroelectricity in both in-plane and out-of-plane directions, even when reduced to a monolayer [68]. The bandgap of α-In_2Se_3 shows a strong thickness dependence, which is 1.3 eV for bulk [69]. The ferroelectricity and direct bandgap of α-In_2Se_3 make it well suited for applications in infrared optoelectronics. β-In_2Se_3 is predicted to be an indirect-bandgap semiconductor at all thicknesses, with bandgap changes from 1.45 eV (bulk) to 1.5 eV (6.2 nm in thick) [70]. GeSe has a distorted NaCl-type crystalline structure, with an indirect bandgap of 1.10 eV in bulk and a direct bandgap of 1.87 eV in monolayer [71]. The detection wavelength of a GeSe-based optoelectronic sensor is limited to about 1 μm due to its interband transitions, which can be broadened to 1.6 μm by introducing Ge vacancies [72]. The Sn-based narrow-bandgap metal chalcogenides include SnS, SnSe, and $SnSe_2$. Orthorhombic SnS is an anisotropic layered semiconductor. It possesses a mid-infrared direct bandgap of 1.19 eV and an absorption coefficient higher than 10^4 cm^{-1} [73]. SnSe has an orthorhombic lattice configuration, maintaining an indirect bandgap while changing its thickness from bulk (0.89 eV) to monolayer (1.63 eV) [70]. SnSe has a high optical absorption coefficient of about 10^5 cm^{-1}, which is about 1–2 orders of magnitude larger than that of silicon and GaAs [74]. Besides its attractive bandgap and absorption characteristics, SnSe also generates a recorded thermoelectric figure-of-merit of about 2.6 from its anharmonicity, making it well-suited for constructing infrared photothermoelectric optoelectronic sensors [75]. $SnSe_2$ has an indirect bandgap that changes from 1.2 eV (bulk) to 2.04 eV (monolayer) [70]. Theoretical calculation results show that the valence band and conduction band of $SnSe_2$ reside at a point along the line G m and the M point, respectively. When the thickness of $SnSe_2$ is reduced to a monolayer, its valence band becomes flat, increasing the density of tis states. The density of the states of monolayer and bilayer $SnSe_2$ exhibit van Hove singularities [70]. These characteristics enable $SnSe_2$'s high photoabsorption. Tetradymites are an important class of non-transition metal

chalcogenides for infrared optoelectronic sensing and include Bi_2S_3, Bi_2Se_3, Bi_2Te_3, Sb_2Se_3, and Sb_2Te_3. Bi_2S_3, Bi_2Se_3, Bi_2Te_3, and Sb_2Te_3 possess direct bandgaps of 1.3 eV, 0.35 eV, 0.21 eV, and 0.45 eV in bulk, making them ideal for absorbing infrared photons. Moreover, Bi_2Se_3, Bi_2Te_3, and Sb_2Te_3 also exhibit outstanding thermoelectric properties owing to their high electron mobility induced by a strong spin-orbit [76,77]. The combination of a narrow bandgap and high thermoelectric performance makes tetradymites promising for infrared sensing applications.

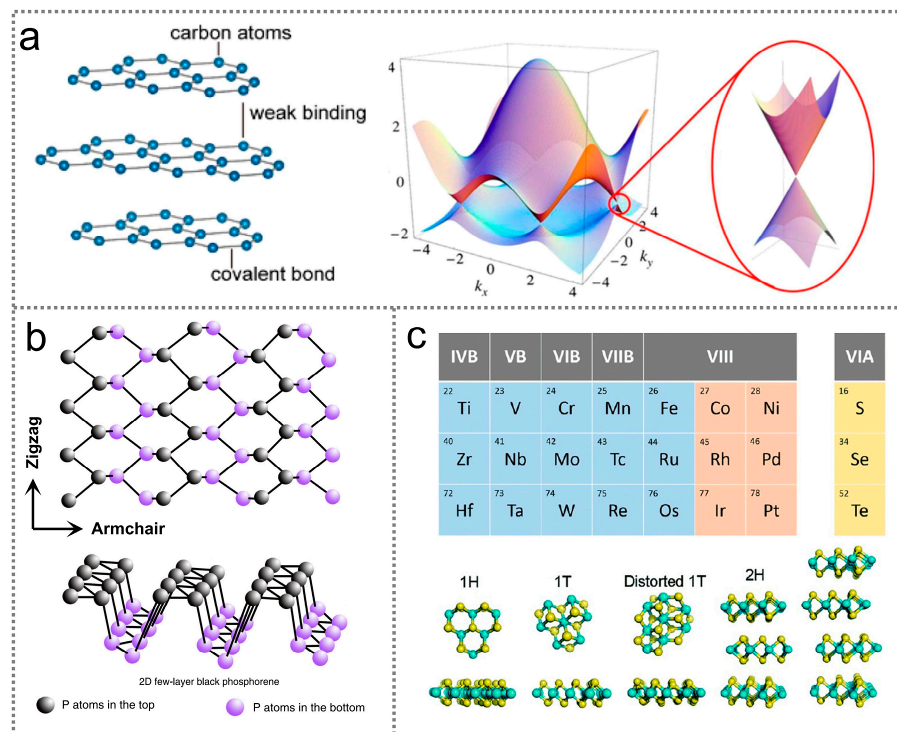

Figure 4. Two-dimensional materials for infrared optoelectronic sensors. (**a**) Atomic structure and band structure of graphene [57] (with permission from the American Chemical Society, 2018). (**b**) Atomic structure of BP [64] (with permission from Springer Nature, 2018). (**c**) Elements for transition metal chalcogenides, and structures of transition metal chalcogenides [78] (with permission from the American Chemical Society, 2021).

Transition metal chalcogenides share the same chemical formula as non-transition metal chalcogenides. However, in transition metal chalcogenides, the M stands for transition metals, such as Mo, W, Hf, and Zr (Figure 4c) [78]. Transition metal chalcogenides can exist in various structures, including 1H, 1T, distorted 1T, 2H, and 3R, where 1T, 2H, and 3R are the most stable and common. The conductivity of transition metal chalcogenides varies greatly with their composition, exhibiting semiconducting or metallic properties. Semiconducting transition metal chalcogenides undergo a transition from an indirect bandgap to a direct bandgap as their thickness decreases to monolayer or bilayer. The bandgaps of typical semiconducting transition metal chalcogenides are in the range of 0.21–2.1 eV [78,79], which can be modulated through strain engineering, electric fields, temperature, and alloying to meet specific demands. For example, DFT calculations predict that the bandgap of monolayer transition metal chalcogenides can be adjusted from 0.68 eV to 2.34 eV through a small tensile strain of 8% [80]. Furthermore, strain can induce an indirect-to-direct bandgap transition in monolayer ZrS_3 and HfS_3. Transition metal dichalcogenides, including MoS_2, $MoSe_2$, $MoTe_2$, WS_2, WSe_2, and $MoTe_2$, are popular materials for infrared sensing because their monolayers exhibit strong light–matter interactions [78]. MoS_2 is one of the most popular transition metal chalcogenides for infrared sensing, with a bandgap ranging from 1.2 eV to 1.9 eV, corresponding to a photodetection of wavelengths of about 0.652–1.033 μm.

Experimental results indicate that monolayer MoS_2 possesses high-field-effect electron and hole mobilities of about 260 $cm^2\ V^{-1}\ s^{-1}$ and 175 $cm^2\ V^{-1}\ s^{-1}$ [81], respectively. This facilitates fast infrared photodetection.

Table 1. Bandgaps of promising 2D semiconductors for infrared optoelectronic sensors.

Material	Bandgap (eV)		Ref.
	Bulk	Monolayer	
Graphene	0	0	[60]
Tellurene	0.325	1.265	[82]
BP	0.3	2.0	[83]
B-AsP	0.3	0.92	[84,85]
InSe	1.26	2.72	[66]
α-In_2Se_3	1.3	1.55	[86]
β-In_2Se_3	0.7	1.29	[87]
SnS	1.19	2.46	[73]
SnSe	0.89	1.63	[70]
$SnSe_2$	1.2	2.04	[72]
Bi_2S_3	1.3	-	[70]
Bi_2Se_3	0.35	-	
Bi_2Te_3	0.21	-	
Sb_2Te_3	0.45	-	
$ZrSe_3$	0.75	1.17	
GeSe	1.1	1.87	[71]
TiS_3	1.02	1.06	[79]
$TiSe_3$	0.21	0.57	
MoS_2	1.2	1.9	[81]
$MoSe_2$	1.1	1.44	[88,89]
$MoTe_2$	0.88	0.90	[90–93]
WS_2	1.3	2.05	[89,94–96]
WSe_2	1.2	1.70	[97,98]
WTe_2	0.7–0.81	0.18	[78]
$ReSe_2$	1.09	1.24	[99]
$PdSe_2$	0.03	1.43	[100]
Bi_2O_2Se	0.8	-	[101]

In addition to the aforementioned 2D materials, transition metal chalcogenophosphates such as $FePS_3$, $FePSe_3$, $Mn_2P_2X_3$, and $Ni_2P_2Te_3$, and Bi-based oxychalcogenides such as Bi_2O_2Se, are also promising candidates for constructing infrared optoelectronic sensors. Furthermore, 2D materials can be utilized in various heterostructures to effectively generate and separate photogenerated electron–hole pairs for infrared sensing. Heterostructures intended for interlayer exciton generation have attracted considerable attention because they break the limits of intrinsic bandgaps. Their interlayer excitons exhibit a lower-energy spectral peak with a much weaker intensity compared to intralayer excitons, granting them a high photoresponse. The performances of advanced infrared optoelectronic sensors based on 2D materials are presented in Table 2.

Table 2. Performance of advanced infrared optoelectronic sensors based on 2D semiconductors.

Active Material	Spectral Range (μm)	Responsivity (A W^{-1})	Specific Detectivity (Jones)	Response Speed (μs)		Ref.
				Rise Time	Fall Time	
Graphene	1.55–11	0.28–38	1×10^9	-	-	[102]
Graphene	5–20	7.62×10^6	6.24×10^{13}			[103]
Antenna/graphene	5.5–7.5	0.27	-	9.5×10^{-3}	-	[104]
Graphene/SnS_2	0.365–2.24	2	1.8×10^{10}	-	-	[105]
Graphene/Si	0.375–3.8	0.1	-	1	-	[106]
Graphene/Si	1.1–4.0	0.003–0.011	1.6×10^{11}	0.02–0.03	-	[107]
Tellurium	0.52–3.0	1.36×10^3	1.15×10^{10}	48.7–62.7	62.7–78.0	[108]
Tellurium	0.83–1.55	6.65×10^3	4.68×10^8	31.7	25.5	[109]
Tellurium	0.635–1.55	9.38	1.19×10^{10}	70	-	[110]
BP	0.52–1.45	1.06	1×10^{11}	-	-	[40]
BP/MoS_2	2.3–3.5	-	1.2×10^{10}	-	-	[111]
B-AsP	0.52–4.6	0.023	2.7×10^{10}	0.4	0.6	[112]
B-AsP	0.98–1.55	1.02×10^4	-	8.2×10^4	9.2×10^4	[113]
InSe	0.976	0.38	-	4.1×10^{-3}	-	[114]
InSe	0.5–1.45	56	5.70×10^{10}	0.17×10^6	-	[115]
InSe/$PdSe_2$	≤1.65	58.8	1×10^{10}	7.2×10^4	1.8×10^5	[116]
α-In_2Se_3	0.325–1.8	1.081×10^3	5.61×10^9	8×10^3	-	[117]
α-In_2Se_3/Si	0.405–0.98	0.56	1.6×10^{13}	43	-	[118]
β-In_2Se_3/Si	0.265–1.3	6.4	4.3×10^{10}	2.2	-	[119]
In_2Se_3	0.59–0.94	5.6	7×10^{10}	1.4×10^5	2.5×10^4	[120]
SnS	0.405–0.808	1.62×10^4	-	3.84×10^4	3.98×10^4	[121]
SnSe	0.532–1.064	1.4×10^{-3}	2.36×10^8	5×10^3	2.8×10^4	[122]
SnSe	0.44–0.85	78.6	9×10^{11}	2.3×10^5	2.7×10^5	[123]
SnSe/InSe	0.405–0.808	0.35	5.8×10^9	2.6×10^5	1.7×10^5	[124]
$SnSe_2$	0.45–1.55	0.761	1.03×10^{12}	2.13×10^4	2.04×10^4	[125]
$SnSe_2$/$MoSe_2$	0.39–1.088	7.09	6.44×10^{12}	2.1×10^5	-	[126]
MoS_2	0.532–1.064	1.65×10^4	-	4.63×10^5	3.15×10^5	[127]
MoS_2	0.473–2.712	0.0475	1.26×10^7	1×10^4	1.6×10^4	[128]
$MoSe_2$/GaAs	0.405–0.808	5.25	1.13×10^{13}	2.9	1.8	[129]
$MoSe_2$	0.52–0.94	2.25	10^{10}	490	495	[130]
$MoTe_2$/MoS_2	0.4–1.48	9.74	-	42	-	[131]
WS_2/Ge	0.2–4.6	0.634	4.3×10^{11}	9.8	12.7	[132]
WSe_2/Si	0.265–1.55	0.689	1.59×10^{12}	0.215	-	[133]
WTe_2	0.32–1.2	8.5×10^{-4}	1.23×10^8	3.2×10^5	3.7×10^5	[134]
Bi_2Se_3/Si	≤0.808	24.28	4.39×10^{12}	2.5	5.5	[135]
Sb_2Se_3/Si	0.43–0.98	-	-	1.6×10^5	2.8×10^5	[136]
Sb_2Te_3/Si	0.405–1.55	0.15	1.65×10^{14}	98	133	[137]
ReS_2/perovskite	0.532–2.0	2.2	1.8×10^{14}	443	720	[138]
$ReSe_2$/$PtSe_2$	0.405–0.98	0.153	7.72×10^{11}	-	-	[139]
$PtSe_2$/Ge	≤1.55	0.766	1.1×10^{11}	54.9	56.6	[140]
$PtTe_2$	0.2–0.98	0.406	3.62×10^{12}	7.51	36.7	[141]
Ta_2NiSe_5/WSe_2	0.532–2.2	10^3	-	1	-	[142]
HgCdTe/BP	0.637–4.3	0.193	7.93×10^{10}	150	110	[143]
SnP_2Se_6	0.78–1.56	10^3	5.1×10^{10}	412	-	[144]

4.2. Group III–V Semiconductor Materials

Group III–V semiconductors with a narrow bandgap have been widely utilized in constructing infrared optoelectronic sensors due to their high carrier mobility, excellent stability, low dielectric constants, and high absorption coefficients [145]. So far, group III–V semiconductor quantum dots, thin films, and single-crystal nanowires have been developed to achieve high-performance infrared sensing. Infrared sensors based on group III–V semiconductor quantum dots and thin films usually exhibit relatively poor performance compared to those based on single-crystal nanowires, because many bulk and surface defects are created in quantum dots and thin films during their fabrication process. Semi-

conductor single-crystal nanowires can transport charge carriers along their axis, reducing carrier scattering and trapping, thereby promoting device performance [146]. Chemical vapor deposition (CVD) is one of the most effective approaches to synthesize high-quality group III–V semiconductor nanowires. For example, InAs nanowires fabricated on Si substrates utilizing the CVD method show an ultra-high carrier mobility of 10^4 cm^2 V^{-1} s^{-1} and an attractive narrow bandgap of about 0.354 eV [147]. $In_xGa_{1-x}As$ nanowires prepared by alloying InAs and GaAs materials exhibit a tunable bandgap (0.35–1.42 eV), meeting their sensors' ever-changing requirements [148]. In particular, $In_{0.65}Ga_{0.35}As$ nanowire materials exhibit a wide spectral response up to 2.0 µm. The light absorption in group III–V semiconductor nanowires such as GaSb and InP nanowires exhibits anisotropy, making them promising for detecting the polarization properties of incident infrared light [149,150].

Since heterojunctions provide a powerful built-in electric field for carrier separation and transport, group III–V single-crystal nanowires have been designed into various heterojunctions, including vertically aligned nanowire homojunctions/heterojunctions, core–shell nanowire heterojunctions, and superlattice structures. For example, a p-i-n homojunction based on InGaAs demonstrates a spectral response from 1.2 µm to 1.7 µm, enabling high-speed optical data reception (32 Gb s^{-1}) [151]. Additionally, a p-n $GaAs_{1-x}Sb_x$/InAs core–shell heterojunction nanowire demonstrates a wide spectral response ranging from 0.488 µm to 1.8 µm, suitable for wide-spectrum photodetection [152]. Infrared optoelectronic sensors based on group III–V semiconductor type-II superlattices have gained significant interest due to their broad-spectrum response, low noise, and high sensitivity. For instance, the GaN/AlN superlattices embedded in GaN nanowires rely on the transitions between quantum-confined electron levels in semiconductor heterostructures, enabling the absorption of light up to 1.63 µm [153]. This structure holds promise for ultrafast and ultrasensitive infrared sensing. Infrared sensors based on various group III–V semiconductors and device structures demonstrate distinct performances, as summarized in Table 3.

Table 3. Performance of advanced infrared optoelectronic sensors based on group III–V semiconductors.

Active Material	Spectral Range (µm)	Responsivity (A W^{-1})	Specific Detectivity (Jones)	Response Speed (µs)		Ref.
				Rise Time	Fall Time	
InGaAs	0.6–1.7	0.53	5.18×10^{11}	-	50.8	[154]
InGaAs	1.2–1.7	0.2	-	-	-	[151]
$In_{0.51}Ga_{0.49}As$	≤1.55	7300	4.2×10^{10}	480	810	[155]
InSb	0.637–4.3	311.5	9.8×10^9	4.2×10^6	5.5×10^6	[156]
InAs	2.0–3.5	0.44	1.25×10^{10}	25	24	[157]
InAs/$SnBr_2$	0.98–1.1	0.36	-	13.5	9	[158]
$GaAs_{1-x}Sb_x$/InAs	0.488–1.8	0.12	-	4.5×10^3	-	[152]
InAs/GaAs	1–3.5	-	2×10^8	-	-	[159]
InSb	≤5.3	-	8.8×10^9	-	-	[160]
GaSb/GeS	0.405–1.31	0.061	6.8×10^{11}	2×10^6	1.2×10^4	[161]
$In_xGa_{1-x}Sb$	0.532–1.55	6×10^3	3.7×10^9	38	53	[162]
InGaAsSb	≤2.2	2.9×10^{-6}	7.4×10^{11}	-	-	[163]
$In_{0.28}Ga_{0.72}Sb$	≤1.55	1.52×10^3	-	13	16	[164]
InGaAs	≤1.6	6.5×10^3	-	7×10^4	2.8×10^5	[148]
GaAsSb	≤1.31	1.7×10^3	-	6×10^4	-	[155]
InGaAs	≤1.55	7.3×10^3	4.2×10^{10}	480	-	[165]
GaSb	≤1.55	77.3	1.14×10^{10}	-	-	[166]
In-rich InGaAs	≤1.55	5.75	-	-	-	[167]
GaAsSb/GaAs	≤0.9	110	1.1×10^{14}	-	-	[168]
GaN/AlN	≤1.55	1.1	-	-	-	[153]

4.3. Ferroelectric Materials

Ferroelectric materials are a key group for the fabrication of infrared optoelectronic sensors due to their remarkable pyroelectric effect and anomalous photovoltaic effect. Compared with other types of pyroelectric materials, ferroelectric materials possess unique advantages, such as high pyroelectric coefficients, excellent chemical and mechanical stability, and low manufacture costs [169]. Moreover, some ferroelectric materials possess a narrow bandgap, making them suitable for simultaneously utilizing pyroelectric and photovoltaic effects to detect infrared light. Ferroelectric $LiTaO_3$ single-crystal materials possess a high Curie temperature, excellent stability, and a high pyroelectric coefficient, making them benchmark materials for infrared sensing applications [170]. Single-crystal materials based on a lead magnesium niobate–lead titanate solid solution system, $xPbMg_{1/3}Nb_{2/3}O_3$-$(1-x)PbTiO_3$ (PMN-PT), have been developed as promising candidates for detecting infrared light. The high pyroelectric coefficient ($\geq$500 μC m^{-2} K^{-1}) of PMN-PT materials was first presented by Davis et al. [171]. Since then, many efforts have been made to develop PMN-PT infrared optoelectronic sensors. The pyroelectric coefficient of a PMN-PT single crystal with a PMN:PT molar ratio of 72:28 is 7.5×10^{-4} C m^{-2} K at room temperature, enabling infrared sensing over the entire infrared region [33]. Ferroelectric $LiNbO_3$ (LNO) materials are important functional materials for constructing integrated optics, nonlinear optics, and optoelectronic devices. Due to their high pyroelectric coefficient of -40 μC m^{-2} K^{-1}, LNO materials exhibit a highly sensitive infrared response [172]. Heterostructures based on LNO and graphene materials can have a wide spectral response region (0.405 μm to 2 μm).

A recently emerging class of ferroelectric materials for infrared sensing applications is that of the molecular perovskite materials, which possess infinite structural flexibility, such as metal-halide perovskites, metal formates, and metal-free molecules [173]. Perovskite ferroelectric $(IA)_2(EA)_2Pb_3Cl_{10}$, where IA and EA stand for isoamylammonium and ethylammonium, respectively, shows almost unchanged dielectric constants over a wide range of temperatures, exhibiting exceptional pyroelectricity [9]. The pyroelectric effect in $(IA)_2(EA)_2Pb_3Cl_{10}$ materials enables their high photoresponse to wavelengths up to 1.95 μm. Aside from their high pyroelectricity, some ferroelectric materials exhibit a narrow energy bandgap, which makes them ideal functional materials for photon-type and hybrid-type infrared optoelectronic sensors. For example, ferroelectric $YMnO_3$ (YMO) materials with a hexagonal structure possess a narrow bandgap (of about 1.55 eV), thereby having the potential for infrared optoelectronic sensing based on their photovoltaic and photoconductive effects [174]. However, driven by a totally different geometric force, YMO materials exhibit a small remnant polarization (5 μC cm^{-2}), leading to a weak photoresponse. Bi doping can greatly increase the ferroelectricity of YMO materials while maintaining an almost unchanged bandgap, therefore promoting their pyroelectric and photovoltaic responses to infrared light. Infrared optoelectronic sensors based on YMO materials show a wide response region with wavelengths up to at least 0.9 μm. Most oxide ferroelectric materials have bandgaps that are usually larger than 2 eV, causing a weak or absent photovoltaic current when responding to infrared light. To solve this problem, a +2 valence d^8 cation substitution at the B site of ABO_3-type perovskite ferroelectrics has been utilized to effectively decrease the bandgap. For instance, Ni^{2+}-doped ferroelectric $0.9KNbO_3$-$0.1(BaNi_{1/2}Nb_{1/2}O_{3-\delta})$ exhibits a narrow direct bandgap of 1.39 eV, enabling infrared sensing by generating photovoltaic signals [175]. Moreover, Ni-modified ferroelectric lead lanthanum zirconate titanate (PLZT) materials exhibit two new absorption peaks in the range of 0.6–1.0 μm and 1.0–1.2 μm compared to pristine PLZT, which has a large bandgap of about 3.3 eV, allowing for infrared optoelectronic sensing [176]. Table 4 summarizes the key metrics of advanced infrared optoelectronic sensors constructed based on ferroelectric materials.

Table 4. Performance of advanced infrared optoelectronic sensors based on ferroelectric materials.

Active Material	Spectral Range (μm)	Responsivity (A W^{-1})	Specific Detectivity (Jones)	Response Speed (μs)		Ref.
				Rise Time	Fall Time	
$(IA)_2(EA)_2Pb_3Cl_{10}$	0.266–1.95	-	-	-	-	[9]
PMN-PT	0.375–118.8	1.64×10^{-8}	-	-	-	[33]
YMO	0.365–0.9	0.6	2.5×10^{12}	400	300	[174]
PLZT	≤1.3	1.64×10^{-7}	4.05×10^{7}	-	-	[176]
YMO/graphene	6–10	-	1.14×10^{5}	1.3×10^{6}	-	[177]
LNO	0.405–2	2.92×10^{6}	8.6×10^{14}	2.3×10^{4}	2.3×10^{4}	[178]
BZT-BCT	0.3–2.5	5.32×10^{-8}	1.49×10^{5}	-	-	[179]
$LuMnO_3$	≤0.9	0.39	6.89×10^{11}	1.44×10^{4}	1.64×10^{4}	[180]
$BiFeO_3$	0.005–0.808	1.8×10^{3}	-	6.97×10^{3}	1.2×10^{3}	[181]

4.4. Organic Semiconductor Materials

Organic semiconductor materials are appealing candidates for constructing infrared optoelectronic sensors due to their intrinsic flexibility, light weight, low cost, scalability and ease of fabrication [8]. Additionally, organic semiconductor materials allow for cooling-free infrared sensing, thereby having great potential for future wearable devices. Significant efforts have been made to explore suitable organic semiconductors for high-performance infrared optoelectronic sensors. Currently, research on organic semiconductor materials for infrared optoelectronic sensors mainly focuses on developing narrow-bandgap organic polymers and small molecules.

To obtain narrow-bandgap polymer materials, a variety of methods have been developed, including donor–acceptor structures, chemical rigidification, quinone structures, and inductive and mesomeric effects. Of these methods, donor–acceptor structures and quinone structures are most used. Donor–acceptor-structured polymers can be fabricated by polymerizing donor and acceptor units. During the polymerization process, two new highest occupied molecular orbital (HOMO) energy levels, together with two new lowest unoccupied molecular orbital (LUMO) energy levels, are generated, forming organic polymers which have narrower bandgaps with higher HOMO and lower LUMO energy levels. Organic polymers with quinone structures can be synthesized by breaking the aromatic units in their backbone and converting the broken aromatic units into double-bond linkages to achieve narrower bandgaps.

The first narrow-bandgap organic polymer for infrared optoelectronic sensing was reported in 2007, which is a new kind of ester group-modified polythieno[3,4-b]thiophene (PTT) [182]. The absorption onset of the fabricated PTT films possesses a bandgap of 1.3 eV, making them well-suited for detecting infrared light with a wavelength less than about 0.95 μm. In 2009, poly(5,7-bis(4-decanyl-2-thienyl)-thieno(3,4-b)diathiazole-thiophene-2,5), with a narrow bandgap of approximately 0.8 eV, was developed for highly sensitive infrared sensing applications, extending the photoresponse region of organic polymer materials to about 1.45 μm [183]. An organic D-A copolymer PBBTPD composed of a donating dithienopyrrole group and a strong accepting benzobisthiadiazole unit shows an absorption onset at 2.5 μm and was presented in 2018, greatly extending the infrared spectral response range [184]. Since then, many other narrow-bandgap polymers have been synthesized for infrared optoelectronic sensing, such as polypyrrole nanoparticles, PTTQn(HD), PBTTT, diketopyrrolopyrrole DPP-based polymer PDPP-DTT, indanone-condensed thiadiazolo[3,4-g]quinoxaline-based polymer PBTTQCN-TT, and PDPP3T:PC_{61}BM [185–189].

Compared to polymers, organic small molecules possess superior characteristics such as high carrier mobility, well-defined structures, and excellent reproducibility. A variety of narrow-bandgap small molecules have been developed for infrared sensing by utilizing various units within different molecular frameworks. Of these small molecules, phthalocyanines are the conventional materials used for constructing infrared optoelectronic sensors. The frequently utilized phthalocyanines include copper phthalocyanine,

copper hexadecafluorophthalocyanine, lead phthalocyanine (PbPc), zinc phthalocyanine, phthalocycanine, vanadylphthalocyanine, tin phthalocyanine, and chloroaluminum phthalocyanine [190–197]. Another important kind of infrared-sensitive small molecules is the group of porphyrin-based compounds. For example, the porphyrin small molecule DHTBTEZP shows a good response in the near infrared region. More advanced infrared optoelectronic sensors based on organic materials are presented in Table 5.

Table 5. Performance of advanced infrared optoelectronic sensors based on organic semiconductors.

Active Material	Spectral Range (μm)	Responsivity (A W^{-1})	Specific Detectivity (Jones)	Response Speed (μs)		Ref.
				Rise Time	Fall Time	
PPy-NPs	0.8–2	1.3	-	130	203	[186]
PBTTT:$PC_{71}BM$	0.75–1	0.05	-	-	-	[187]
PBTTT:$PC_{61}BM$	0.775–1.075	-	-	-	-	[187]
PDPP-DTT	0.808–1.55	2×10^3	-	1.8×10^5	1.5×10^5	[188]
PDPP3T:$PC_{61}BM$	0.405–0.85	-	7.8×10^{13}	2.24×10^4	6.8×10^3	[189]
TPBi:PDPP3T:$PC_{61}BM$	0.405–0.85	-	4.49×10^{14}	1.09×10^4	4.5×10^3	[189]
PDPP3T:PS:$PC_{61}BM$	0.405–0.85	-	1.52×10^{14}	2.31×10^4	9.4×10^3	[189]
TPBi:PDPP3T:PS:$PC_{61}BM$	0.405–0.85	-	5.43×10^{14}	5.3×10^3	1.8×10^3	[189]
η-$F_{16}CuPc$	0.589–0.94	-	-	4.48×10^5	4.48×10^5	[191]
PbPc	0.9–1	0.035	-	-	-	[192]
ZnMe2Pc	0.698–0.79	0.013	-	-	-	[193]
$8OH_2Pc$	$\leq$0.77	-	2.1×10^{12}	-	-	[194]
SnPc	0.405–0.98	7.2×10^{-4}	6.98×10^9	-	-	[196]
ClAlPc	$\leq$0.78	-	5.8×10^{12}	0.75	0.7	[197]
CDT-TQ:$PC_{71}BM$	0.4–1.4	0.1	7.8×10^9	167	-	[198]
CO1-4Cl	0.92–0.96	0.5	3.1×10^{13}	-	-	[199]
PBBTCD	0.8–1.2	4×10^{-4}	-	51	55	[200]
TQ-T:IEICO-4F	0.35–1.8	8.4×10^{-6}	10^{10}	-	-	[201]
BDP-OMe:C_{60}	0.3–0.9	-	10^{13}	-	-	[202]
CPDT-TQ:$PC_{71}BM$	0.9–1.31	-	5×10^{10}	-	-	[203]

4.5. Others

Aside from the abovementioned advanced materials, which have been extensively researched, some other materials have also been utilized to construct high-performance infrared optoelectronic sensors, such as mercury chalcogenides and organic–inorganic hybrid perovskite semiconductors. Mercury chalcogenides exhibit unique ultra-broad and tunable photoresponses across the near-infrared and mid-infrared regions, demonstrating an optoelectronic sensing performance comparable to commercial devices and particularly advantageous at high operating temperatures [204]. Among the various mercury chalcogenides, HgCdTe shows a broad tunability of its absorption spectrum (3–12 μm) and a long photocarrier lifetime (up to 1 μs), having remained the leading material for infrared detection for years. HgCdTe emerged as a photoconductive material with a performance comparable to that of InSb in 1959 [205]. Its bandgap can be conveniently adjusted by controlling the Hg to Cd ratio. Recently, HgTe nanocrystals have been proven to be promising materials capable of replacing the bandgap tunability of HgCdTe alloys, transitioning from mixed composition to quantum confinement. The bandgap of HgTe materials can be modulated from 1.5 eV to almost 0.02 eV [204]. Organic–inorganic hybrid perovskite semiconductors have been considered one of the most promising materials for infrared sensing applications due to their long excitation diffusion length, high charge carrier mobility, direct bandgap, and high absorption coefficient [206]. The performance of state-of-the-art infrared optoelectronic sensors based on diverse mercury chalcogenide quantum dots and organic–inorganic hybrid perovskite semiconductors is provided in Table 6.

Table 6. Performance of advanced infrared optoelectronic sensors based on mercury chalcogenide quantum dots and organic–inorganic hybrid perovskite semiconductors.

	Active Material	Spectral Range (μm)	Responsivity ($A\ W^{-1}$)	Specific Detectivity (Jones)	Response Speed (μs)		Ref.
					Rise Time	Fall Time	
Mercury chalcogenide	HgCdTe/graphene	4	2.5	2×10^{10}	0.013	-	[207]
	HgTe	≤2.6	1	$>10^{10}$	-	-	[208]
	HgTe	≤2.5	0.25	1.5×10^{10}	1	-	[209]
	HgTe	≤2.3	0.023	3.2×10^{6}	-	-	[210]
	HgTe	≤4.8	0.23	5.4×10^{10}	0.9	2	[211]
	HgTe	≤2.5	10^{3}	10^{12}	20	-	[212]
	HgTe	≤4	0.7	2×10^{10}	11	-	[213]
	HgTe	≤4	0.32	7×10^{10}	0.07	-	[214]
	HgTe-P3HT	2.5	1	$>10^{11}$	-	1.5	[215]
	HgTe-graphene	≤3	150	6×10^{8}	400	700	[216]
	HgTe p-n junction	≤2.5	2×10^{-3}	-	-	3×10^{-3}	[217]
	HgTe/Ag_2Te	≤3–5	1.62	4×10^{11}	<1	-	[218]
	HgTe/HgTe	≤2.5	0.02	3×10^{9}	-	0.37	[219]
	Bi_2Se_3/HgTe/Ag_2Te	≤2.5	0.22	7.5×10^{10}	-	-	[220]
	Bi_2Se_3/HgTe/Ag_2Te	1.5–2.1	0.2	$>10^{10}$	0.12	-	[221]
	SnO_2/HgTe/Ag_2Te	≤2	0.3	5×10^{10}	0.3	-	[222]
	$CdSe_2$/HgTe/Ag_2Te	≤2	0.8	9×10^{10}	0.17	-	[223]
	HgSe	≤4.2	0.077	1.7×10^{9}	-	-	[224]
	HgSe/HgTe	≤4	0.003	10^{9}	0.17	0.15	[225]
Hybrid perovskite	$MAPbI_3$/Gd-ZnO	0.25–1.357	0.22	9.3×10^{9}	4×10^{5}	5×10^{5}	[226]
	$MAPbI_xCl_{3-x}$/Si	0.3–1.15	0.87	6×10^{12}	5×10^{4}	1.5×10^{5}	[227]
	$MAPbI_3$/CuO	0.35–1.05	0.562	2.15×10^{13}	2×10^{5}	2×10^{5}	[228]
	$MAPbI_3$/PbSe	0.3–2.6	0.628	2.59×10^{12}	4	32	[229]
	$MAPbI_3$/$CuInSe_2$	0.3–1.1	0.15	7.7×10^{11}	0.277	0.277	[230]
	$MAPbI_{2.5}Br_{0.5}$/PbS	0.4–1.4	0.99	4×10^{12}	<10	<10	[231]
	$MAPbI_3$/PDPPTDTPT	0.35–1.05	-	1×10^{11}	6.1×10^{-3}	6.1×10^{-3}	[232]
	$MAPbI_3$	0.4–1	4	-	39	1.9	[233]
	$FA_{0.85}Cs_{0.15}PbI_3$/Bi_2Se_3	0.3–1	1.02	2.08×10^{12}	16	14	[234]
	$MAPbI_3$/SnPc	0.3–1	0.72×10^{-3}	6.98×10^{9}	390	530	[196]
	$MAPbI_3$/MoS_2	0.5–0.85	110	7.93×10^{7}	6.17×10^{6}	4.5×10^{6}	[235]
	$MAPbI_3$/PbSe	0.3–1.5	0.7	7×10^{7}	2.5×10^{3}	3×10^{3}	[236]
	$MAPbI_{3-x}Cl_x$/PbS	0.3–1.5	0.35	9×10^{10}	250	500	[237]
	$MAPbI_{3-x}(SCN)_x$/Si	0.35–1.1	13	1×10^{13}	22.2	17.6	[238]
	$MASnI_3$	0.2–1	0.47	8.8×10^{10}	1.5×10^{6}	4×10^{5}	[239]
	$FASnI_3$	0.3–1	2×10^{3}	3.2×10^{12}	-	-	[240]
	$FA_{0.85}Cs_{0.15}Sn_{0.5}Pb_{0.5}I$	0.6–1	0.53	6×10^{12}	5.83×10^{-2}	0.86	[241]
	$(FASnI_3)_{0.6}(MAPbI_3)_{0.4}$	0.3–1	0.4	1.1×10^{12}	6.9	9.1	[242]
	$MA_{0.5}FA_{0.5}Pb_{0.5}Sn_{0.5}I_3$	0.35–1	>0.2	$>10^{12}$	-	-	[243]
	$MASn_xPb_{1-x}I_3$	0.3–1.1	0.2	$>10^{11}$	0.09	2.27	[244]
	$(CsPbI_3)_{0.05}(FAPbI_3)_{1-x}$	0.405–0.81	84.77	3.22×10^{12}	2.46×10^{4}	1.47×10^{4}	[245]

Notes: "MA" stands for methylammonium CH_3NH_3. "FA" stands for formamidinium $CHNH_3$.

5. Applications

Infrared optoelectronic sensors have become deeply integrated into modern technology and human society, with applications spanning image sensing, optical neuromorphic computing, logic operations, and health monitoring.

5.1. Image Sensing

Imaging sensing is one of the most widespread applications of infrared optoelectronic sensors, and a large number of image devices based on different materials have been developed. For instance, a highly sensitive infrared optoelectronic image sensor has been developed utilizing a two-dimensional Bi_2O_2Se crystal exhibiting a high sensitivity of

65 AW^{-1} at 1.2 μm and an ultrafast response speed of about 1 ps at room temperature [246]. Figure 5a illustrates the schematic diagram and the performance of a single pixel of the Bi_2O_2Se infrared image sensor. The device demonstrates a broadband response with a spectrum ranging from visible to 1.7 μm. Scanning a laser beam over the sensor results in a photovoltage distribution, generating electrical signals with opposite polarities at its Bi_2O_2Se/metal interfaces, indicating that the electrical signals are primarily produced by photogenerated carrier separation at the symmetric Bi_2O_2Se/metal interfaces. Bi_2O_2Se infrared image sensors can be fabricated on a flexible mica substrate and consistently deliver a photocurrent even if undergoing a bending process with a strain of 1%. Moreover, these devices exhibit a non-attenuating photocurrent after more than 4 weeks, indicating their excellent stability in the ambient environment. When illuminated by lasers with different wavelengths (1.55 μm, 1.31 μm, 1.2 μm, and 0.655 μm), the photocurrent generated from a 3 × 5 multi-pixel Bi_2O_2Se sensor array can clearly show the laser beam's distribution (Figure 5a).

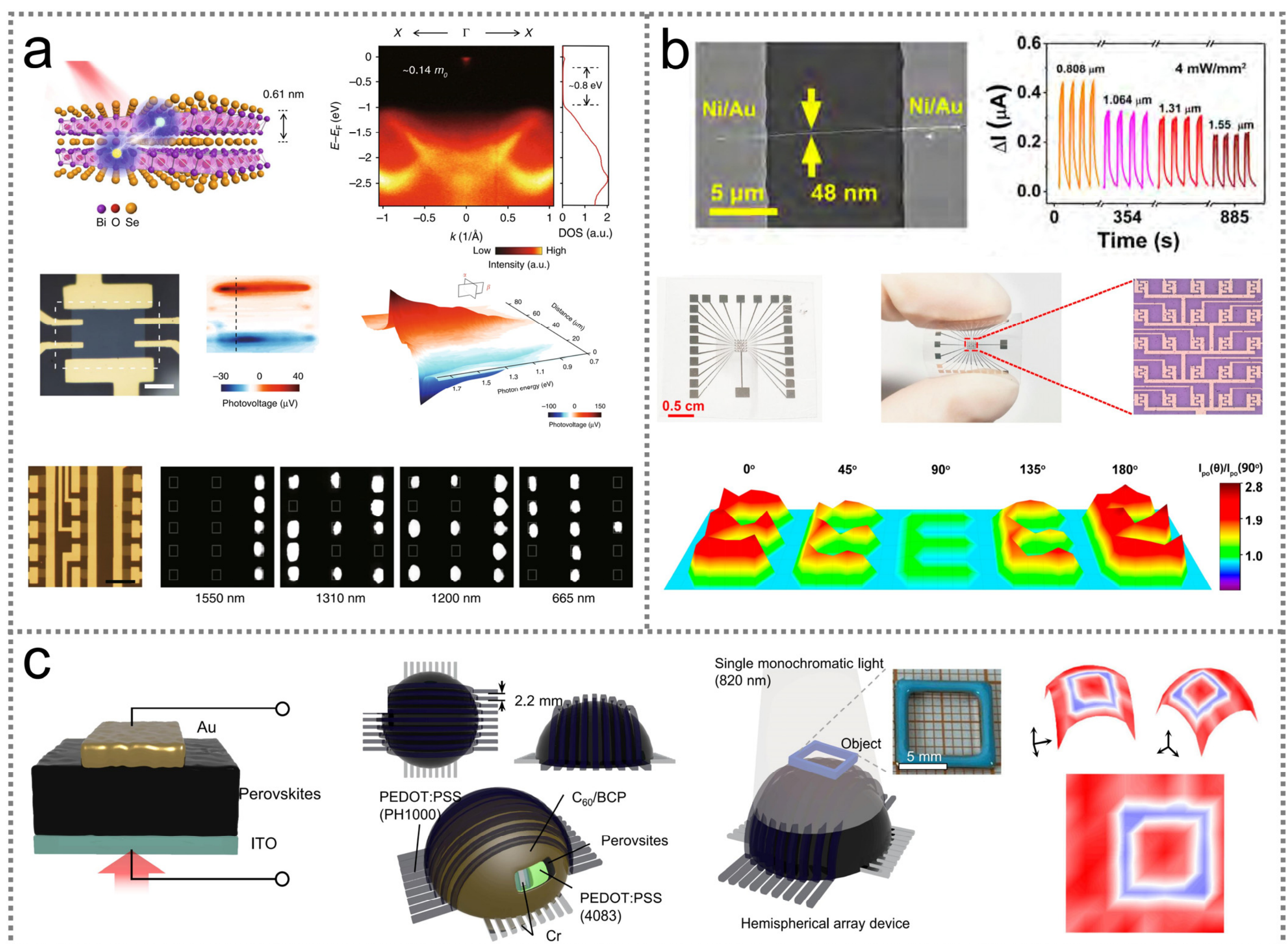

Figure 5. Infrared optoelectronic sensors for image sensing. (**a**) Infrared optoelectronic sensor based on Bi_2O_2Se for image sensing [246] (with permission from Springer Nature, 2018). (**b**) Device design and performance of an infrared polarimetric image sensor [149] (with permission from the American Chemical Society, 2022). (**c**) A hemispherical infrared optoelectronic sensor based on perovskites for wide-angle imaging sensing [247] (with permission from Springer Nature, 2022).

Infrared polarimetric image sensors are capable of extending their detection of photoelectric signals from light wavelength and intensity to the light's polarization vector, exhibiting great potential in the fields of remote image sensing, medical diagnosis, and environmental monitoring. Figure 5b exhibits an infrared polarimetric image sensor constructed utilizing sulfur-passivated GaSb nanowire arrays [149]. This 5×5 GaSb sensor array with interdigital electrodes is fabricated on a flexible PET substrate. One single pixel demonstrates a high responsivity of 9.39×10^2 A W^{-1}, an ultrahigh detectivity of 1.10×10^{11} Jones, a high dichroic ratio of 2.65, and a wide spectral response from 0.808 µm to 1.55 µm. With the assistance of a hollow mask "E", linear polarization light with a wavelength of 1.55 µm can be illustrated on the GaSb sensor array within the "E" area. The output three-dimensional images show a clear "E" pattern, with polarization angles of 0° and 180° stronger than those of 45°, 90°, and 135°, demonstrating its significant near-infrared polarization imaging ability.

In addition to the abovementioned flat image sensors, infrared optoelectronic sensors can also be designed in a hemispherical shape for wide-angle imaging applications, as illustrated in Figure 5c [247]. A hemispherical image sensor with 9×9 pixels can be constructed based on photosensitive phenylethylammonium/formamidinium lead halide perovskite materials using a spray-coating method. The device can capture images at various wavelengths, with a wide incident light angle of 180°.

5.2. Optical Neuromorphic Computing

Neuromorphic optoelectronic sensors, which utilize artificial photosensitive synapses, are capable of emulating biological nervous systems, with in-memory sensing and computing abilities. Based on a planar heterostructure composed of perylene and graphene oxide, optoelectronic sensors exhibit a broadband photoperception range from 0.365 µm to 1.55 µm and an ultrahigh specific detectivity of 3.1×10^{13} Jones [248]. Figure 6a exhibits the schematic diagram and performance of the sensor, where a type-II band structure is formed at the perylene/graphene oxide interface due to the energy level mismatch in the perylene and graphene oxide materials. The perylene/graphene oxide heterostructure can effectively absorb photons and separate photogenerated electron–hole pairs for photoelectric signal generation. Upon illumination, the sensor is able to emulate visual perception and diverse synaptic plasticity, including biological neurons, with the features of an excitatory postsynaptic current, spike-intensity-dependent plasticity, spike-number-dependent plasticity, and short-/long-term memories. When a pattern image is fed into a 10×10 perylene/graphene oxide array, the weighted graphs of the learning patterns become more and more distinct with the light pulse number, facilitating image recognition. By utilizing the sensor array as a neuron, the accuracy of an artificial neural network for image classification can reach 85%. Additionally, infrared optoelectronic sensors can also be utilized for edge computing (in-sensor computing), significantly reducing communication latency and energy consumption for artificial vision in distributed systems and robotic devices. As illustrated in Figure 6b, a BP-based programmable phototransistor optoelectronic sensor is capable of being programmed with 5-bit precision to perform an in-sensor convolutional neural network, with a high accuracy of 92%, by electrically and optically modulating the stored charges in its gate dielectrics [249].

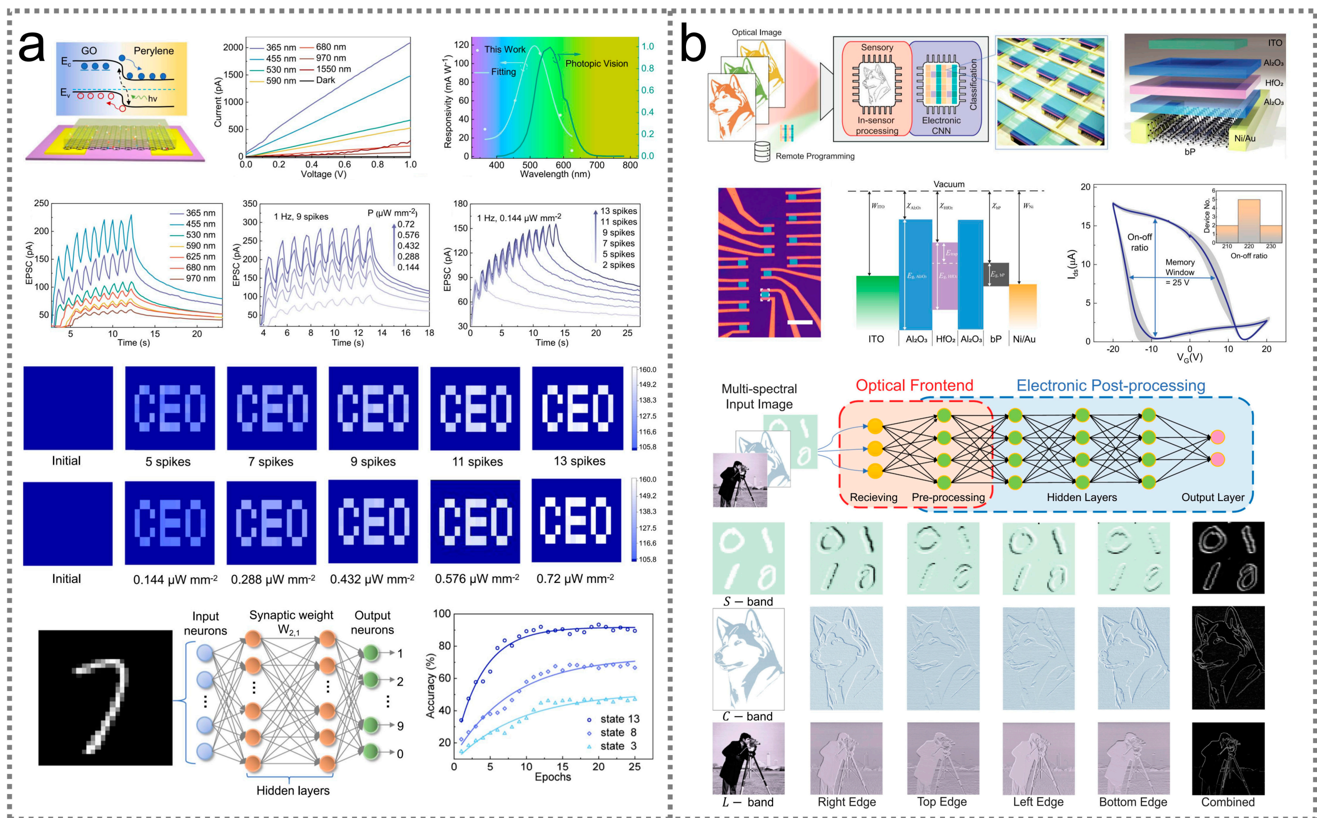

Figure 6. Infrared optoelectronic sensor for neuromorphic computing. (**a**) Device design, photonic synaptic characteristics, and image memorization and recognition capability of an infrared optoelectronic sensor based on a perylene/graphene oxide heterostructure [248] (with permission from Springer Nature, 2022). (**b**) Device configuration, current-voltage characteristics, and in-sensor computing performance of an infrared optoelectronic sensor based on black phosphorus materials [249] (with permission from Springer Nature, 2022).

5.3. Logic Operation

The growing demand for a wide range of data processing has driven interest toward optoelectronic logic gate platforms because of their broad bandwidth and fast data transmission. An optoelectronic sensor based on a back-to-back p+-i-n-p-p+ diode structure exhibits a bipolar spectral photoresponse to visible and infrared light [250]. As illustrated in Figure 7, the sensor consists of vertically stacked low-bandgap (1.21 eV) perovskite $FA_{0.5}MA_{0.5}Pb_{0.4}Sn_{0.6}I_3$ for infrared photon adsorption, and a large-bandgap (1.67 eV) perovskite $MAPbI_3$ for visible photon adsorption. When illuminated by visible and infrared light, the sensor generates currents with positive and negative polarities, respectively, paving the way for optical logic gate operations. By controlling the wavelength and intensity of the incident light, a single sensor can achieve five basic logic operations "OR", "AND", "NAND", "NOR", and "NOT". For instance, the sensor executes an "AND" operation when illuminated with visible light (0.625 μm at 0.6 mW cm^{-2}) combined with intensity-varying near-infrared light (0.94 μm).

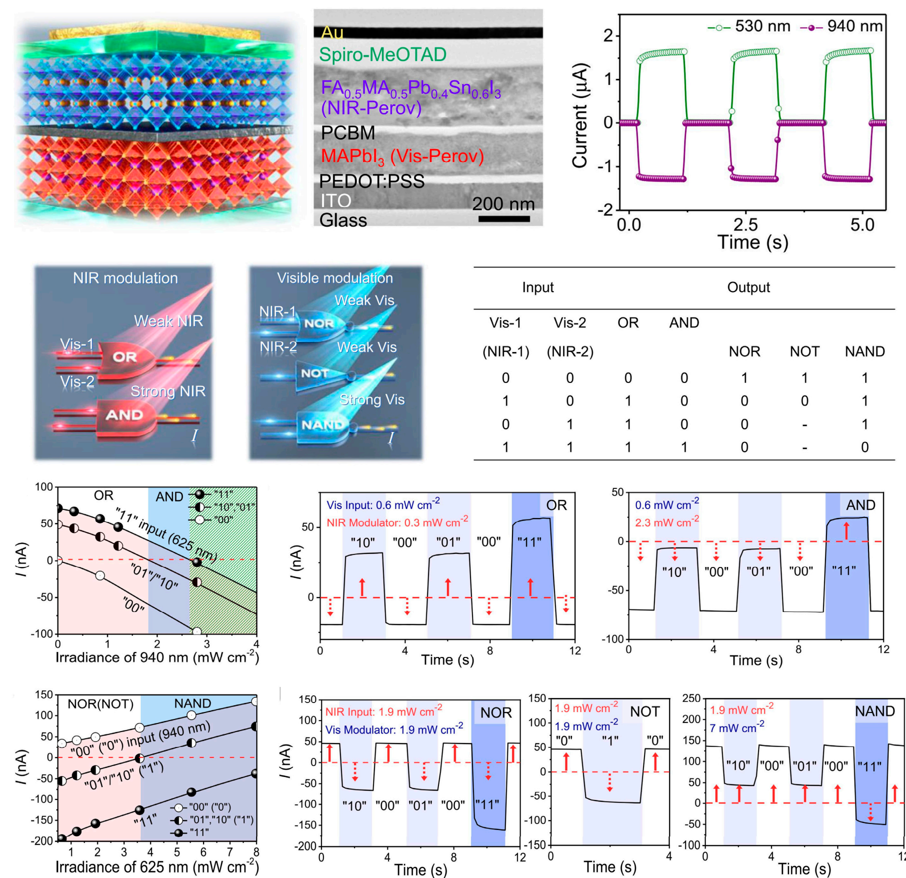

Figure 7. Device design and outputs of a perovskite infrared optoelectronic sensor for logic operations. The device can achieve the five basic logic operations of "OR", "AND", "NAND", "NOR", and "NOT" by controlling the wavelength and intensity of its incident lights [250] (with permission from Springer Nature, 2022).

5.4. Health Monitoring

Infrared optoelectronic sensors provide an effective approach to monitoring health conditions, particularly blood pulse frequency and blood oxygen saturation (SpO_2). Figure 8a shows a metal halide perovskites-based flexible optoelectronic sensor, which can be utilized for blood pulse signal detection based on photoplethysmography [251]. The basic working principle of the sensor can be described as follows: When light with a wavelength of 0.8 μm is incident on the fingertip, a part of the light is absorbed, reflected, and scattered by human tissues, and then transmits through the finger to enter the flexible optoelectronic sensor. During this process, the light intensity measured by the sensor fluctuates with the variations in the volume of the blood vessels, induced by the heartbeat. The contraction of the heart leads to an increase in the blood volume in the vessels, thereby decreasing the detectable light's intensity. Conversely, the diastole of the heart results in a decreased blood volume in the vessels, hence increasing the detectable light's intensity. In this way, the heart rate can be extracted from the generated electrical signals of the sensor for cardiopulmonary function evaluations. When the light is turned on, reproducible electrical signals can be observed due to the periodic contraction and diastole of the human heart, from which a patient's blood pulse frequency can be derived according to the electrical signal's frequency. An infrared optoelectronic sensor for SpO_2 monitoring is illustrated in Figure 8b [252]. This optoelectronic sensor is fabricated based on a PffBT4T-2OD:PC_{71}BM heterostructure, which exhibits a high detectivity of 7.2×10^{12} Jones at 0.85 μm. According to the Beer–Lambert law, SpO_2 can be derived from the difference in transmission at specific wavelengths of light utilizing the equation [252,253]

$$\mathrm{S_pO_2} = \frac{\varepsilon_{\mathrm{Hb}}(\lambda_{625}) - \varepsilon_{\mathrm{Hb}}(\lambda_{850})R_{\mathrm{os}}}{[\varepsilon_{\mathrm{Hb}}(\lambda_{625}) - \varepsilon_{\mathrm{HbO_2}}(\lambda_{625})] + [\varepsilon_{\mathrm{HbO_2}}(\lambda_{850}) - \varepsilon_{\mathrm{Hb}}(\lambda_{850})R_{\mathrm{os}}]} \quad (11)$$

where $\varepsilon_{\mathrm{Hb}}$ and $\varepsilon_{\mathrm{HbO2}}$ stand for the molar extinction coefficients of oxyhemoglobin and deoxyhemoglobin, respectively. R_{os} can be obtained from the ratio of the pulsatile (AC) and stationary (DC) parts of the photoplethysmogram signals utilizing the formula [252,253]

$$R_{\mathrm{OS}} = \frac{AC_{850}/DC_{850}}{AC_{625}/DC_{625}} \quad (12)$$

Due to its broadband photoresponse, the PffBT4T-2OD:$PC_{71}BM$ optoelectronic sensor exhibits distinct photocurrent signals under the illumination of both 0.625 μm and 0.85 μm wavelengths, achieving SpO_2 detection.

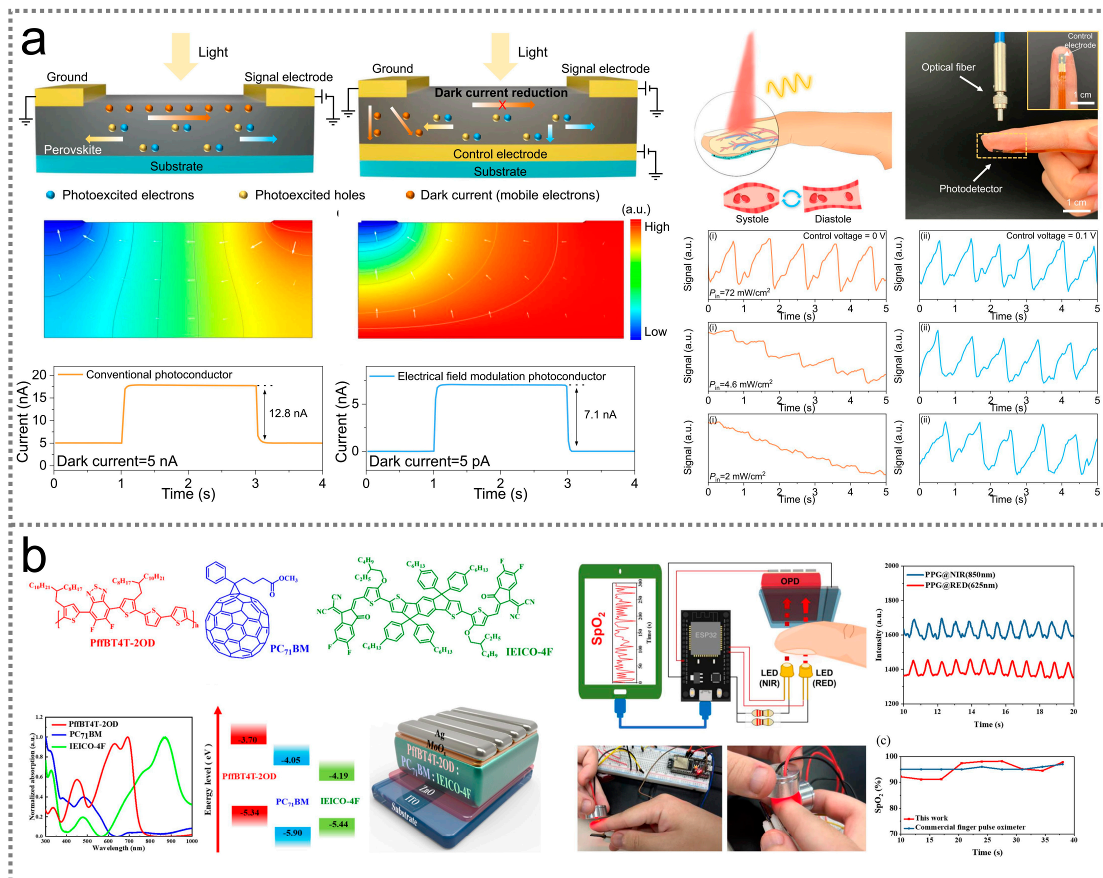

Figure 8. Infrared optoelectronic sensors for health monitoring. (**a**) Device configuration, working mechanism, and outputs of a perovskite infrared optoelectronic sensor for detecting blood pulse frequency [251] (with permission from Springer Nature, 2023). (**b**) Device structure and outputs of an organic infrared optoelectronic sensor for monitoring blood oxygen saturation [252] (with permission from the American Chemical Society, 2023).

5.5. Others

In addition to the aforementioned applications, infrared optoelectronic sensors also demonstrate potential applications in optical communication and gas sensing. Figure 9a illustrates a photothermoelectric infrared optoelectronic sensor used for optical communication applications [254]. The sensor is fabricated utilizing tellurium nanoribbons. By converting its polarization-sensitive absorption into a large temperature gradient with the assistance of the finite-size effects of perfect plasmonic absorbers, the sensor shows advantages including a high responsivity (410 V W^{-1}) and ultrahigh polarization ratio

(2.5×10^4) that make it well suited for polarization-coded communication. During the communication process, mid-infrared light can first be converted into American Standard Code for Information Interchange (ASCII) codes by varying the polarization angle, with 0° for "0" and 90° for "1", respectively. In this way, the input signals can be encoded by the polarization-sensitive sensor and finally fed into a terminal computer. The received signals match well with the input signals, demonstrating the capability of the sensor for information transmission. Figure 9b illustrates an infrared optoelectronic sensor for gas sensing applications [255]. The device is composed of a single-mode $Ge_{28}Sb_{12}Se_{60}$ waveguide, a graphene channel, split graphene back-gates, and HfO_2 gate dielectrics. The graphene back-gates can be utilized to electrostatically create a p-n junction along the center of the graphene channel. The sensor enables NO detection at concentrations comparable to the recommended exposure limit of 25 ppm, which pushes forward the development of gas sensing microsystems.

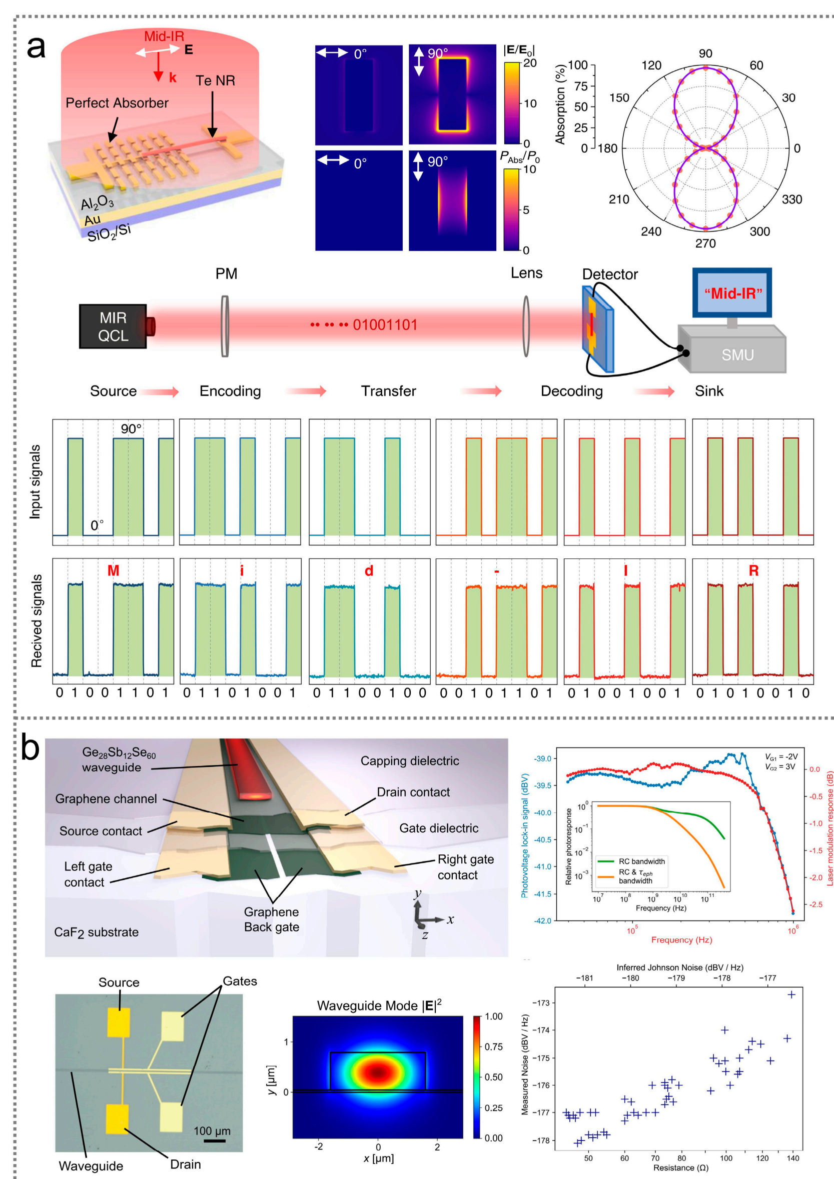

Figure 9. Infrared optoelectronic sensors for optical communication and gas sensing. (**a**) Device design and polarization-coded communication process of a polarization-sensitive infrared optoelectronic sensor [254] (with permission from Springer Nature, 2023). (**b**) Schematic diagram, frequency response, and measured noise spectral density of a graphene-based infrared optoelectronic sensor for gas sensing [255] (with permission from Springer Nature, 2022).

6. Conclusions and Prospects

In this review, we summarized the current status of infrared optoelectronic sensors. Based on their working mechanisms, these sensors can be roughly classified into three categories: photon, photothermal, and hybrid sensors. Two-dimensional semimetals and semiconductors, group III–V semiconductors, ferroelectric materials, and organic semiconductors exhibit unique advantages in infrared optoelectronic sensing. For instance, 2D semimetals and semiconductors are suitable for high-speed photodetection due to their high carrier mobility, and ferroelectric materials have the potential to simultaneously utilize pyroelectric and photovoltaic effects for an enhanced photoresponse. Embedded deeply in modern technology and human society, infrared optoelectronic sensors show promise in diverse applications, including image sensing, neuromorphic computing, logic operations, optical communication, health monitoring, and gas sensing.

While plenty of advancements have been made in exploring infrared optoelectronic sensors, several challenges remain in this field. (1) The response speed of most existing infrared optoelectronic sensors is in the order of microseconds, which is insufficient for capturing rapidly changing light. (2) Comprehensive characterizations of infrared optoelectronic sensors, including their response range, responsivity, specific detectivity, response time, NEP, LDR, and EQE, are needed for the further optimization of these devices. (3) Although some infrared optoelectronic sensors have been utilized for health monitoring applications, research on their biocompatibility is lacking.

Considering the growing demand for high-performance infrared optoelectronic sensors, various research directions could be pursued to advance the development of infrared optoelectronic sensors in the near future. (1) Most 2D materials for infrared optoelectronic sensors are fabricated based on small-size mechanically exfoliated flakes, so it is essential to develop techniques for their scalable production. The most promising methods to achieve large-scale 2D materials might be CVD and molecular beam epitaxy. (2) Infrared optoelectronic sensors based on narrow-bandgap semiconductors usually exhibit unstable performances due to variations in ambient temperature, hence developing temperature-insensitive devices is of great importance. Micro-constant temperature systems which can be integrated into infrared optoelectronic sensors can help solve this problem. (3) The development of optical logic operations and optical communication pose new challenges for high-frequency devices; therefore, ultrafast infrared optoelectronic sensors are desirable. To achieve this, materials with ultrahigh carrier mobility and homo-/heterostructures with strong built-in electric fields are required. (4) The investigation of biocompatible infrared optoelectronic sensors is promising for future healthcare. This might be realized using non-toxic organic semiconductors. (5) In optical neuromorphic computing applications, the development of photosynapses with a long memory, for weight storage, is essential. Carrier trapping using device interfaces or ferroelectric polarization are promising for achieving this goal. Overall, the development of infrared optoelectronic sensors will contribute to advancements in daily life, industry, and the medical field, and more efforts are needed to further improve their performance.

Author Contributions: X.Y. retrieved the literature and wrote the review. X.Y., Y.J. and X.S. edited and proofread the manuscript and organized the diagrams. Y.J. and X.L. supervised this project. All authors have read and agreed to the published version of the manuscript.

Funding: This research was funded by the National Natural Science Foundation of China, grant numbers 12075024 and 11875084.

Conflicts of Interest: The authors declare no conflicts of interest.

References

1. Elbanna, A.; Jiang, H.; Fu, Q.; Zhu, J.-F.; Liu, Y.; Zhao, M.; Liu, D.; Lai, S.; Chua, X.W.; Pan, J.; et al. 2D Material Infrared Photonics and Plasmonics. *ACS Nano* **2023**, *17*, 4134–4179. [CrossRef]
2. Koppens, F.H.L.; Mueller, T.; Avouris, P.; Ferrari, A.C.; Vitiello, M.S.; Polini, M. Photodetectors Based on Graphene, Other Two-Dimensional Materials and Hybrid Systems. *Nat. Nanotech.* **2014**, *9*, 780–793. [CrossRef]

3. Soref, R. Mid-Infrared Photonics in Silicon and Germanium. *Nat. Photonics* **2010**, *4*, 495–497. [CrossRef]
4. García de Arquer, F.P.; Armin, A.; Meredith, P.; Sargent, E.H. Solution-Processed Semiconductors for Next-Generation Photodetectors. *Nat. Rev. Mater.* **2017**, *2*, 16100. [CrossRef]
5. Xia, F.; Wang, H.; Xiao, D.; Dubey, M.; Ramasubramaniam, A. Two-Dimensional Material Nanophotonics. *Nat. Photonics* **2014**, *8*, 899–907. [CrossRef]
6. Pei, J.; Yang, J.; Yildirim, T.; Zhang, H.; Lu, Y. Many-Body Complexes in 2D Semiconductors. *Adv. Mater.* **2019**, *31*, 1706945. [CrossRef]
7. Vella, J.H.; Huang, L.; Eedugurala, N.; Mayer, K.S.; Ng, T.N.; Azoulay, J.D. Broadband Infrared Photodetection Using a Narrow Bandgap Conjugated Polymer. *Sci. Adv.* **2021**, *7*, eabg2418. [CrossRef]
8. Dou, L.; Liu, Y.; Hong, Z.; Li, G.; Yang, Y. Low-Bandgap Near-IR Conjugated Polymers/Molecules for Organic Electronics. *Chem. Rev.* **2015**, *115*, 12633–12665. [CrossRef]
9. Hua, L.; Wang, J.; Liu, Y.; Guo, W.; Ma, Y.; Xu, H.; Han, S.; Luo, J.; Sun, Z. Improper High-T_c Perovskite Ferroelectric with Dielectric Bistability Enables Broadband Ultraviolet-to-Infrared Photopyroelectric Effects. *Adv. Sci.* **2023**, *10*, 2301064. [CrossRef]
10. Sassi, U.; Parret, R.; Nanot, S.; Bruna, M.; Borini, S.; De Fazio, D.; Zhao, Z.; Lidorikis, E.; Koppens, F.H.L.; Ferrari, A.C.; et al. Graphene-Based Mid-Infrared Room-Temperature Pyroelectric Bolometers with Ultrahigh Temperature Coefficient of Resistance. *Nat. Commun.* **2017**, *8*, 14311. [CrossRef]
11. Long, M.; Gao, A.; Wang, P.; Xia, H.; Ott, C.; Pan, C.; Fu, Y.; Liu, E.; Chen, X.; Lu, W.; et al. Room temperature high-detectivity mid-infrared photodetectors based on black arsenic phosphorus. *Sci. Adv.* **2017**, *3*, e1700589. [CrossRef]
12. Wu, F.; Li, Q.; Wang, P.; Xia, H.; Wang, Z.; Wang, Y.; Luo, M.; Chen, L.; Chen, F.; Miao, J.; et al. High Efficiency and Fast van der Waals Hetero-Photodiodes with a Unilateral Depletion Region. *Nat. Commun.* **2019**, *10*, 4663. [CrossRef]
13. Huo, N.; Konstantatos, G. Ultrasensitive All-2D MoS_2 Phototransistors Enabled by an Out-of-Plane MoS_2 PN Homojunction. *Nat. Commun.* **2017**, *8*, 572. [CrossRef]
14. Wu, E.; Wu, D.; Jia, C.; Wang, Y.; Yuan, H.; Zeng, L.; Xu, T.; Shi, Z.; Tian, Y.; Li, X. In Situ Fabrication of 2D WS_2/Si Type-II Heterojunction for Self-Powered Broadband Photodetector with Response up to Mid-Infrared. *ACS Photonics* **2019**, *6*, 565–572. [CrossRef]
15. Xiao, Z.; Yuan, Y.; Shao, Y.; Wang, Q.; Dong, Q.; Bi, C.; Sharma, P.; Gruverman, A.; Huang, J. Giant Switchable Photovoltaic Effect in Organometal Trihalide Perovskite Devices. *Nat. Mater.* **2015**, *14*, 193–198. [CrossRef]
16. Sobhani, A.; Knight, M.W.; Wang, Y.; Zheng, B.; King, N.S.; Brown, L.V.; Fang, Z.; Nordlander, P.; Halas, N.J. Narrowband Photodetection in the Near-Infrared with a Plasmon-induced Hot Electron Device. *Nat. Commun.* **2013**, *4*, 1643. [CrossRef]
17. Tang, X.; Ackerman, M.M.; Chen, M.; Guyot-Sionnest, P. Dual-Band Infrared Imaging Using Stacked Colloidal Quantum Dot Photodiodes. *Nat. Photonics* **2019**, *13*, 277–282. [CrossRef]
18. Choi, M.-J.; García de Arquer, F.P.; Proppe, A.H.; Seifitokaldani, A.; Choi, J.; Kim, J.; Baek, S.-W.; Liu, M.; Sun, B.; Biondi, M.; et al. Cascade Surface Modification of Colloidal Quantum Dot Inks Enables Efficient Bulk Homojunction Photovoltaics. *Nat. Commun.* **2020**, *11*, 103. [CrossRef]
19. Chen, M.; Xue, X.; Qin, T.; Wen, C.; Hao, Q.; Tang, X. Universal Homojunction Design for Colloidal Quantum Dot Infrared Photodetectors. *Adv. Mater. Technol.* **2023**, *8*, 2300315. [CrossRef]
20. Mitta, S.B.; Ali, F.; Yang, Z.; Moon, I.; Ahmed, F.; Yoo, T.J.; Lee, B.H.; Yoo, W.J. Gate-Modulated Ultrasensitive Visible and Near-Infrared Photodetection of Oxygen Plasma-Treated WSe_2 Lateral pn-Homojunctions. *ACS Appl. Mater. Interfaces* **2020**, *12*, 23261–23271. [CrossRef]
21. Li, C.; Tian, R.; Chen, X.; Gu, L.; Luo, Z.; Zhang, Q.; Yi, R.; Li, Z.; Jiang, B.; Liu, Y.; et al. Waveguide-Integrated $MoTe_2$ p-i-n Homojunction Photodetector. *ACS Nano* **2022**, *16*, 20946–20955. [CrossRef]
22. Ji, Y.; Wu, L.; Liu, Y.; Yang, Y. Chemo-Phototronic Effect Induced Electricity for Enhanced Self-Powered Photodetector System Based on ZnO Nanowires. *Nano Energy* **2021**, *89*, 106449. [CrossRef]
23. Yang, X.; Liu, X.; Qu, L.; Gao, F.; Xu, Y.; Cui, M.; Yu, H.; Wang, Y.; Hu, P.; Feng, W. Boosting Photoresponse of Self-Powered InSe-Based Photoelectrochemical Photodetectors via Suppression of Interface Doping. *ACS Nano* **2022**, *16*, 8440–8448. [CrossRef]
24. Dai, M.; Chen, H.; Feng, R.; Feng, W.; Hu, Y.; Yang, H.; Liu, G.; Chen, X.; Zhang, J.; Xu, C.-Y.; et al. A Dual-Band Multilayer InSe Self-Powered Photodetector with High Performance Induced by Surface Plasmon Resonance and Asymmetric Schottky Junction. *ACS Nano* **2018**, *12*, 8739–8747. [CrossRef]
25. Afzal, A.M.; Dastgeer, G.; Iqbal, M.Z.; Gautam, P.; Faisal, M.M. High-Performance p-BP/n-$PdSe_2$ Near-Infrared Photodiodes with a Fast and Gate-Tunable Photoresponse. *ACS Appl. Mater. Interfaces* **2020**, *12*, 19625–19634. [CrossRef]
26. Zhang, K.; Zhang, T.; Cheng, G.; Li, T.; Wang, S.; Wei, W.; Zhou, X.; Yu, W.; Sun, Y.; Wang, P.; et al. Interlayer Transition and Infrared Photodetection in Atomically Thin Type-II $MoTe_2$/MoS_2 van der Waals Heterostructures. *ACS Nano* **2016**, *10*, 3852–3858. [CrossRef]
27. Tang, L.; Kocabas, S.E.; Latif, S.; Okyay, A.K.; Ly-Gagnon, D.-S.; Saraswat, K.C.; Miller, D.A.B. Nanometre-Scale Germanium Photodetector Enhanced by a Near-Infrared Dipole Antenna. *Nat. Photonics* **2008**, *2*, 226–229. [CrossRef]
28. Fang, H.; Hu, W. Photogating in Low Dimensional Photodetectors. *Adv. Sci.* **2017**, *4*, 1700323. [CrossRef]
29. Bowen, C.R.; Taylor, J.; LeBoulbar, E.; Zabek, D.; Chauhan, A.; Vaish, R. Pyroelectric Materials and Devices for Energy Harvesting Applications. *Energ. Environ. Sci.* **2014**, *7*, 3836–3856. [CrossRef]

30. Wang, X.; Dai, Y.; Liu, R.; He, X.; Li, S.; Wang, Z.L. Light-Triggered Pyroelectric Nanogenerator Based on a pn-Junction for Self-Powered Near-Infrared Photosensing. *ACS Nano* **2017**, *11*, 8339–8345. [CrossRef]
31. Dao, T.D.; Ishii, S.; Yokoyama, T.; Sawada, T.; Sugavaneshwar, R.P.; Chen, K.; Wada, Y.; Nabatame, T.; Nagao, T. Hole Array Perfect Absorbers for Spectrally Selective Midwavelength Infrared Pyroelectric Detectors. *ACS Photonics* **2016**, *3*, 1271–1278. [CrossRef]
32. Zhu, Y.; Wang, B.; Deng, C.; Wang, Y.; Wang, X. Photothermal-Pyroelectric-Plasmonic Coupling for High Performance and Tunable Band-Selective Photodetector. *Nano Energy* **2021**, *83*, 105801. [CrossRef]
33. Fang, H.; Xu, C.; Ding, J.; Li, Q.; Sun, J.-L.; Dai, J.-Y.; Ren, T.-L.; Yan, Q. Self-Powered Ultrabroadband Photodetector Monolithically Integrated on a PMN-PT Ferroelectric Single Crystal. *ACS Appl. Mater. Interfaces* **2016**, *8*, 32934–32939. [CrossRef]
34. Pandya, S.; Wilbur, J.; Kim, J.; Gao, R.; Dasgupta, A.; Dames, C.; Martin, L.W. Pyroelectric Energy Conversion with Large Energy and Power Density in Relaxor Ferroelectric Thin films. *Nat. Mater.* **2018**, *17*, 432–438. [CrossRef]
35. Yang, M.-M.; Luo, Z.-D.; Mi, Z.; Zhao, J.; Pei, S.E.; Alexe, M. Piezoelectric and Pyroelectric Effects Induced by Interface Polar Symmetry. *Nature* **2020**, *584*, 377–381. [CrossRef]
36. Cai, X.; Sushkov, A.B.; Suess, R.J.; Jadidi, M.M.; Jenkins, G.S.; Nyakiti, L.O.; Myers-Ward, R.L.; Li, S.; Yan, J.; Gaskill, D.K.; et al. Sensitive Room-Temperature Terahertz Detection via the Photothermoelectric Effect in Graphene. *Nat. Nanotech.* **2014**, *9*, 814–819. [CrossRef]
37. Huang, D.; Zou, Y.; Jiao, F.; Zhang, F.; Zang, Y.; Di, C.-a.; Xu, W.; Zhu, D. Interface-Located Photothermoelectric Effect of Organic Thermoelectric Materials in Enabling NIR Detection. *ACS Appl. Mater. Interfaces* **2015**, *7*, 8968–8973. [CrossRef]
38. Cao, F.; Liu, L.; Li, L. Short-Wave Infrared Photodetector. *Mater. Today* **2023**, *62*, 327–349. [CrossRef]
39. Cutler, M.; Mott, N.F. Observation of Anderson Localization in an Electron Gas. *Phys. Rev.* **1969**, *181*, 1336. [CrossRef]
40. Wu, S.; Chen, Y.; Wang, X.; Jiao, H.; Zhao, Q.; Huang, X.; Tai, X.; Zhou, Y.; Chen, H.; Wang, X.; et al. Ultra-sensitive Polarization-Resolved Black Phosphorus Homojunction Photodetector Defined by Ferroelectric Domains. *Nat. Commun.* **2022**, *13*, 3198. [CrossRef]
41. Rogalski, A.; Antoszewski, J.; Faraone, L. Third-Generation Infrared Photodetector Arrays. *J. Appl. Phys.* **2009**, *105*, 091101. [CrossRef]
42. Zhang, T.; Ren, Z.; Guo, S.; Zhang, G.; Wang, S.; Qiao, S. Broadband Self-Powered CdS ETL-Based $MAPbI_3$ Heterojunction Photodetector Induced by a Photovoltaic-Pyroelectric-Thermoelectric Effect. *ACS Appl. Mater. Interfaces* **2023**, *15*, 44444–44455. [CrossRef]
43. Ma, J.; Chen, M.; Qiao, S.; Chang, J.; Fu, G.; Wang, S. Photovoltaic-Pyroelectric Coupled Effect in Ag_2Se/Si Heterojunction for Broad-Band, Ultrafast, Self-Powered, Position-Sensitive Detectors. *ACS Photonics* **2022**, *9*, 2160–2169. [CrossRef]
44. Huo, N.; Konstantatos, G. Recent Progress and Future Prospects of 2D-Based Photodetectors. *Adv. Mater.* **2018**, *30*, 1801164. [CrossRef]
45. Morteza Najarian, A.; Vafaie, M.; Chen, B.; García de Arquer, F.P.; Sargent, E.H. Photophysical Properties of Materials for High-Speed Photodetection. *Nat. Rev. Phys.* **2024**, *6*, 219–230. [CrossRef]
46. Zeng, L.; Han, W.; Ren, X.; Li, X.; Wu, D.; Liu, S.; Wang, H.; Lau, S.P.; Tsang, Y.H.; Shan, C.-X.; et al. Uncooled Mid-Infrared Sensing Enabled by Chip-Integrated Low-Temperature-Grown 2D $PdTe_2$ Dirac Semimetal. *Nano Lett.* **2023**, *23*, 8241–8248. [CrossRef]
47. Zhao, Z.; Dong, F.; Wang, Y.; Sun, J.; Ye, H.; Wang, R.; Zhang, J. Growth of Few-Layer WTe_2 by a Salt-Assisted Double-Tube Chemical Vapor Deposition Method with High Infrared Photosensitivity. *Nanoscale* **2023**, *15*, 11955–11962. [CrossRef]
48. Long, M.; Wang, P.; Fang, H.; Hu, W. Progress, Challenges, and Opportunities for 2D Material Based Photodetectors. *Adv. Funct. Mater.* **2019**, *29*, 1803807. [CrossRef]
49. Liu, J.; Xia, F.; Xiao, D.; García de Abajo, F.J.; Sun, D. Semimetals for High-Performance Photodetection. *Nat. Mater.* **2020**, *19*, 830–837. [CrossRef]
50. Sun, D.; Wu, Z.-K.; Divin, C.; Li, X.; Berger, C.; de Heer, W.A.; First, P.N.; Norris, T.B. Ultrafast Relaxation of Excited Dirac Fermions in Epitaxial Graphene Using Optical Differential Transmission Spectroscopy. *Phys. Rev. Lett.* **2008**, *101*, 157402. [CrossRef]
51. Guo, Q.; Pospischil, A.; Bhuiyan, M.; Jiang, H.; Tian, H.; Farmer, D.; Deng, B.; Li, C.; Han, S.-J.; Wang, H.; et al. Black Phosphorus Mid-Infrared Photodetectors with High Gain. *Nano Lett.* **2016**, *16*, 4648–4655. [CrossRef]
52. Nidhi; Jakhar, A.; Uddin, W.; Kumar, J.; Nautiyal, T.; Das, S. Nanolayered Black Arsenic-Silicon Lateral Heterojunction Photodetector for Visible to Mid-Infrared Wavelengths. *ACS Appl. Nano Mater.* **2020**, *3*, 9401–9409. [CrossRef]
53. Li, J.; Wang, Z.; Wen, Y.; Chu, J.; Yin, L.; Cheng, R.; Lei, L.; He, P.; Jiang, C.; Feng, L.; et al. High-Performance Near-Infrared Photodetector Based on Ultrathin Bi_2O_2Se Nanosheets. *Adv. Funct. Mater.* **2018**, *28*, 1706437. [CrossRef]
54. Shen, C.; Liu, Y.; Wu, J.; Xu, C.; Cui, D.; Li, Z.; Liu, Q.; Li, Y.; Wang, Y.; Cao, X.; et al. Tellurene Photodetector with High Gain and Wide Bandwidth. *ACS Nano* **2020**, *14*, 303–310. [CrossRef]
55. Chen, Y.; Xi, J.; Dumcenco, D.O.; Liu, Z.; Suenaga, K.; Wang, D.; Shuai, Z.; Huang, Y.-S.; Xie, L. Tunable Band Gap Photoluminescence from Atomically Thin Transition-Metal Dichalcogenide Alloys. *ACS Nano* **2013**, *7*, 4610–4616. [CrossRef]
56. Novoselov, K.S.; Geim, A.K.; Morozov, S.V.; Jiang, D.; Zhang, Y.; Dubonos, S.V.; Grigorieva, I.V.; Firsov, A.A. Electric Field Effect in Atomically Thin Carbon Films. *Science* **2004**, *306*, 666–669. [CrossRef] [PubMed]
57. Lin, L.; Deng, B.; Sun, J.; Peng, H.; Liu, Z. Bridging the Gap between Reality and Ideal in Chemical Vapor Deposition Growth of Graphene. *Chem. Rev.* **2018**, *118*, 9281–9343. [CrossRef] [PubMed]

58. Lin, J.; Cretu, O.; Zhou, W.; Suenaga, K.; Prasai, D.; Bolotin, K.I.; Cuong, N.T.; Otani, M.; Okada, S.; Lupini, A.R.; et al. Flexible Metallic Nanowires with Self-Adaptive Contacts to Semiconducting Transition-Metal Dichalcogenide Monolayers. *Nat. Nanotech.* **2014**, *9*, 436–442. [CrossRef]
59. Chen, J.-H.; Cullen, W.G.; Jang, C.; Fuhrer, M.S.; Williams, E.D. Defect Scattering in Graphene. *Phys. Rev. Lett.* **2009**, *102*, 236805. [CrossRef]
60. Giannazzo, F.; Sonde, S.; Nigro, R.L.; Rimini, E.; Raineri, V. Mapping the Density of Scattering Centers Limiting the Electron Mean Free Path in Graphene. *Nano Lett.* **2011**, *11*, 4612–4618. [CrossRef]
61. Zhang, Y.; Ma, C.; Xie, J.; Ågren, H.; Zhang, H. Black Phosphorus/Polymers: Status and Challenges. *Adv. Mater.* **2021**, *33*, 2100113. [CrossRef] [PubMed]
62. Xia, F.; Wang, H.; Jia, Y. Rediscovering Black Phosphorus as an Anisotropic Layered Material for Optoelectronics and Electronics. *Nat. Commun.* **2014**, *5*, 4458. [CrossRef]
63. Wang, X.; Jones, A.M.; Seyler, K.L.; Tran, V.; Jia, Y.; Zhao, H.; Wang, H.; Yang, L.; Xu, X.; Xia, F. Highly Anisotropic and Robust Excitons in Monolayer Black Phosphorus. *Nat. Nanotech.* **2015**, *10*, 517–521. [CrossRef]
64. You, H.; Jia, Y.; Wu, Z.; Wang, F.; Huang, H.; Wang, Y. Room-Temperature Pyro-Catalytic Hydrogen Generation of 2D Few-Layer Black Phosphorene under Cold-Hot Alternation. *Nat. Commun.* **2018**, *9*, 2889. [CrossRef] [PubMed]
65. Kim, H.; Uddin, S.Z.; Lien, D.-H.; Yeh, M.; Azar, N.S.; Balendhran, S.; Kim, T.; Gupta, N.; Rho, Y.; Grigoropoulos, C.P.; et al. Actively Variable-Spectrum Optoelectronics with Black Phosphorus. *Nature* **2021**, *596*, 232–237. [CrossRef]
66. Tamalampudi, S.R.; Lu, Y.-Y.; Kumar, R.U.; Sankar, R.; Liao, C.-D.; Moorthy, B.K.; Cheng, C.-H.; Chou, F.C.; Chen, Y.-T. High Performance and Bendable Few-Layered InSe Photodetectors with Broad Spectral Response. *Nano Lett.* **2014**, *14*, 2800–2806. [CrossRef] [PubMed]
67. Jang, H.; Seok, Y.; Choi, Y.; Cho, S.-H.; Watanabe, K.; Taniguchi, T.; Lee, K. High-Performance Near-Infrared Photodetectors Based on Surface-Doped InSe. *Adv. Funct. Mater.* **2021**, *31*, 2006788. [CrossRef]
68. Xue, F.; Hu, W.; Lee, K.-C.; Lu, L.-S.; Zhang, J.; Tang, H.-L.; Han, A.; Hsu, W.-T.; Tu, S.; Chang, W.-H.; et al. Room-Temperature Ferroelectricity in Hexagonally Layered α-In_2Se_3 Nanoflakes down to the Monolayer Limit. *Adv. Funct. Mater.* **2018**, *28*, 1803738. [CrossRef]
69. Hou, P.; Wang, X.; Liu, Y.; Chen, Y.; Dong, S.; Guo, H.; Wang, J.; Zhong, X.; Ouyang, X. A Neutron Irradiation-Induced Displacement Damage of Indium Vacancies in α-In_2Se_3 Nanoflakes. *Phys. Chem. Chem. Phys.* **2020**, *22*, 15799–15804. [CrossRef]
70. Wang, F.; Wang, Z.; Yin, L.; Cheng, R.; Wang, J.; Wen, Y.; Shifa, T.A.; Wang, F.; Zhang, Y.; Zhan, X.; et al. 2D Library beyond Graphene and Transition Metal Dichalcogenides: A Focus on Photodetection. *Chem. Soc. Rev.* **2018**, *47*, 6296–6341. [CrossRef]
71. Shi, G.; Kioupakis, E. Anisotropic Spin Transport and Strong Visible-Light Absorbance in Few-Layer SnSe and GeSe. *Nano Lett.* **2015**, *15*, 6926–6931. [CrossRef]
72. He, T.; Wang, Z.; Cao, R.; Li, Q.; Peng, M.; Xie, R.; Huang, Y.; Wang, Y.; Ye, J.; Wu, P.; et al. Extrinsic Photoconduction Induced Short-Wavelength Infrared Photodetectors Based on Ge-Based Chalcogenides. *Small* **2021**, *17*, 2006765. [CrossRef]
73. Zhang, Z.; Yang, J.; Zhang, K.; Chen, S.; Mei, F.; Shen, G. Anisotropic Photoresponse of Layered 2D SnS-Based near Infrared Photodetectors. *J. Mater. Chem. C* **2017**, *5*, 11288–11293. [CrossRef]
74. Minnam Reddy, V.R.; Gedi, S.; Pejjai, B.; Park, C. Perspectives on SnSe-Based Thin Film Solar Cells: A Comprehensive Review. *J. Mater. Sci. Mater. Electron.* **2016**, *27*, 5491–5508. [CrossRef]
75. Zhao, L.-D.; Lo, S.-H.; Zhang, Y.; Sun, H.; Tan, G.; Uher, C.; Wolverton, C.; Dravid, V.P.; Kanatzidis, M.G. Ultralow Thermal Conductivity and High Thermoelectric Figure of Merit in SnSe Crystals. *Nature* **2014**, *508*, 373. [CrossRef]
76. Zhang, H.; Liu, C.-X.; Qi, X.-L.; Dai, X.; Fang, Z.; Zhang, S.-C. Topological Insulators in Bi_2Se_3, Bi_2Te_3 and Sb_2Te_3 with a Single Dirac Cone on the Surface. *Nat. Phys.* **2009**, *5*, 438–442. [CrossRef]
77. Heremans, J.P.; Cava, R.J.; Samarth, N. Tetradymites as Thermoelectrics and Topological Insulators. *Nat. Rev. Mater.* **2017**, *2*, 17049. [CrossRef]
78. Sun, Y.; Niu, G.; Ren, W.; Meng, X.; Zhao, J.; Luo, W.; Ye, Z.-G.; Xie, Y.-H. Hybrid System Combining Two-Dimensional Materials and Ferroelectrics and Its Application in Photodetection. *ACS Nano* **2021**, *15*, 10982–11013. [CrossRef]
79. Jin, Y.; Li, X.; Yang, J. Single layer of MX_3 (M = Ti, Zr; X = S, Se, Te): A New Platform for Nano-Electronics and Optics. *Phys. Chem. Chem. Phys.* **2015**, *17*, 18665–18669. [CrossRef]
80. Li, M.; Dai, J.; Zeng, X.C. Tuning the Electronic Properties of Transition-Metal Trichalcogenides via Tensile Strain. *Nanoscale* **2015**, *7*, 15385–15391. [CrossRef]
81. Liu, Y.; Guo, J.; Zhu, E.; Liao, L.; Lee, S.-J.; Ding, M.; Shakir, I.; Gambin, V.; Huang, Y.; Duan, X. Approaching the Schottky-Mott Limit in van der Waals Metal-Semiconductor Junctions. *Nature* **2018**, *557*, 696–700. [CrossRef]
82. Wood, J.D.; Wells, S.A.; Jariwala, D.; Chen, K.-S.; Cho, E.; Sangwan, V.K.; Liu, X.; Lauhon, L.J.; Marks, T.J.; Hersam, M.C. Effective Passivation of Exfoliated Black Phosphorus Transistors against Ambient Degradation. *Nano Lett.* **2014**, *14*, 6964–6970. [CrossRef]
83. He, J.; He, D.; Wang, Y.; Cui, Q.; Bellus, M.Z.; Chiu, H.-Y.; Zhao, H. Exceptional and Anisotropic Transport Properties of Photocarriers in Black Phosphorus. *ACS Nano* **2015**, *9*, 6436–6442. [CrossRef]
84. Xia, F.; Wang, H.; Hwang, J.C.M.; Neto, A.H.C.; Yang, L. Black Phosphorus and Its Isoelectronic Materials. *Nat. Rev. Phys.* **2019**, *1*, 306–317. [CrossRef]
85. Zhou, W.; Zhang, S.; Wang, Y.; Guo, S.; Qu, H.; Bai, P.; Li, Z.; Zeng, H. Anisotropic In-Plane Ballistic Transport in Monolayer Black Arsenic-Phosphorus FETs. *Adv. Electron. Mater.* **2020**, *6*, 1901281. [CrossRef]

86. Zhou, J.; Zeng, Q.; Lv, D.; Sun, L.; Niu, L.; Fu, W.; Liu, F.; Shen, Z.; Jin, C.; Liu, Z. Controlled Synthesis of High-Quality Monolayered α-In_2Se_3 via Physical Vapor Deposition. *Nano Lett.* **2015**, *15*, 6400–6405. [CrossRef]
87. Debbichi, L.; Eriksson, O.; Lebègue, S. Two-Dimensional Indium Selenides Compounds: An Ab Initio Study. *J. Phys. Chem. Lett.* **2015**, *6*, 3098–3103. [CrossRef]
88. Tongay, S.; Zhou, J.; Ataca, C.; Lo, K.; Matthews, T.S.; Li, J.; Grossman, J.C.; Wu, J. Thermally Driven Crossover from Indirect toward Direct Bandgap in 2D Semiconductors: $MoSe_2$ versus MoS_2. *Nano Lett.* **2012**, *12*, 5576–5580. [CrossRef]
89. Ma, Y.; Dai, Y.; Guo, M.; Niu, C.; Lu, J.; Huang, B. Electronic and Magnetic Properties of Perfect, Vacancy-Doped, and Nonmetal Adsorbed $MoSe_2$, $MoTe_2$ and WS_2 Monolayers. *Phys. Chem. Chem. Phys.* **2011**, *13*, 15546. [CrossRef]
90. Keum, D.H.; Cho, S.; Kim, J.H.; Choe, D.-H.; Sung, H.-J.; Kan, M.; Kang, H.; Hwang, J.-Y.; Kim, S.W.; Yang, H.; et al. Bandgap Opening in Few-Layered Monoclinic $MoTe_2$. *Nat. Phys.* **2015**, *11*, 482–486. [CrossRef]
91. Lin, Y.-F.; Xu, Y.; Wang, S.-T.; Li, S.-L.; Yamamoto, M.; Aparecido-Ferreira, A.; Li, W.; Sun, H.; Nakaharai, S.; Jian, W.-B.; et al. Ambipolar $MoTe_2$ Transistors and Their Applications in Logic Circuits. *Adv. Mater.* **2014**, *26*, 3263–3269. [CrossRef]
92. Lezama, I.G.; Arora, A.; Ubaldini, A.; Barreteau, C.; Giannini, E.; Potemski, M.; Morpurgo, A.F. Indirect-to-Direct Band Gap Crossover in Few-Layer $MoTe_2$. *Nano Lett.* **2015**, *15*, 2336–2342. [CrossRef]
93. Ruppert, C.; Aslan, O.B.; Heinz, T.F. Optical Properties and Band Gap of Single- and Few-Layer $MoTe_2$ Crystals. *Nano Lett.* **2014**, *14*, 6231–6236. [CrossRef]
94. Kam, K.K.; Parkinson, B.A. Detailed Photocurrent Spectroscopy of the Semiconducting Group VIB Transition Metal Dichalcogenides. *J. Phys. Chem.* **1982**, *86*, 463–467. [CrossRef]
95. Li, W.; Wang, T.; Dai, X.; Wang, X.; Zhai, C.; Ma, Y.; Chang, S. Bandgap Engineering of Different Stacking WS_2 Bilayer under an External Electric Field. *Solid State Commun.* **2016**, *225*, 32–37. [CrossRef]
96. Gutierrez, H.R.; Perea-Lopez, N.; Elias, A.L.; Berkdemir, A.; Wang, B.; Lv, R.; Lopez-Urias, F.; Crespi, V.H.; Terrones, H.; Terrones, M. Extraordinary Room-Temperature Photoluminescence in Triangular WS_2 Monolayers. *Nano Lett.* **2013**, *13*, 3447–3454. [CrossRef]
97. Desai, S.B.; Seol, G.; Kang, J.S.; Fang, H.; Battaglia, C.; Kapadia, R.; Ager, J.W.; Guo, J.; Javey, A. Strain-Induced Indirect to Direct Bandgap Transition in Multilayer WSe_2. *Nano Lett.* **2014**, *14*, 4592–4597. [CrossRef]
98. Yun, W.S.; Han, S.W.; Hong, S.C.; Kim, I.G.; Lee, J.D. Thickness and Strain Effects on Electronic Structures of Transition Metal Dichalcogenides: 2H-MX_2 Semiconductors (M = Mo, WX = S, Se, Te). *Phys. Rev. B* **2012**, *85*, 033305. [CrossRef]
99. Yang, S.; Tongay, S.; Li, Y.; Yue, Q.; Xia, J.-B.; Li, S.-S.; Li, J.; Wei, S.-H. Layer-Dependent Electrical and Optoelectronic Responses of $ReSe_2$ Nanosheet Transistors. *Nanoscale* **2014**, *6*, 7226–7231. [CrossRef]
100. Sun, J.; Shi, H.; Siegrist, T.; Singh, D.J. Electronic, Transport, and Optical Properties of Bulk and Mono-Layer $PdSe_2$. *Appl. Phys. Lett.* **2015**, *107*, 153902. [CrossRef]
101. Chen, C.; Wang, M.; Wu, J.; Fu, H.; Yang, H.; Tian, Z.; Tu, T.; Peng, H.; Sun, Y.; Xu, X.; et al. Electronic Structures and Unusually Robust Bandgap in an Ultrahigh-Mobility Layered Oxide Semiconductor, Bi_2O_2Se. *Sci. Adv.* **2018**, *4*, eaat8355. [CrossRef]
102. Jiang, H.; Fu, J.; Wei, J.; Li, S.; Nie, C.; Sun, F.; Wu, Q.Y.S.; Liu, M.; Dong, Z.; Wei, X.; et al. Synergistic-Potential Engineering Enables High-Efficiency Graphene Photodetectors for Near- to Mid-infrared Light. *Nat. Commun.* **2024**, *15*, 1225. [CrossRef]
103. Guo, J.; Liu, Y.; Lin, Y.; Tian, Y.; Zhang, J.; Gong, T.; Cheng, T.; Huang, W.; Zhang, X. Simulation of Tuning Graphene Plasmonic Behaviors by Ferroelectric Domains for Self-Driven Infrared Photodetector Applications. *Nanoscale* **2019**, *11*, 20868–20875. [CrossRef]
104. Castilla, S.; Vangelidis, I.; Pusapati, V.-V.; Goldstein, J.; Autore, M.; Slipchenko, T.; Rajendran, K.; Kim, S.; Watanabe, K.; Taniguchi, T.; et al. Plasmonic Antenna Coupling to Hyperbolic Phonon-Polaritons for Sensitive and Fast Mid-Infrared Photodetection with Graphene. *Nat. Commun.* **2020**, *11*, 4872. [CrossRef]
105. Zhao, Y.; Tsai, T.-Y.; Wu, G.; Ó Coileáin, C.; Zhao, Y.-F.; Zhang, D.; Hung, K.-M.; Chang, C.-R.; Wu, Y.-R.; Wu, H.-C. Graphene/SnS_2 van der Waals Photodetector with High Photoresponsivity and High Photodetectivity for Broadband 365–2240 nm Detection. *ACS Appl. Mater. Interfaces* **2021**, *13*, 47198–47207. [CrossRef]
106. Liu, W.; Lv, J.; Peng, L.; Guo, H.; Liu, C.; Liu, Y.; Li, W.; Li, L.; Liu, L.; Wang, P.; et al. Graphene Charge-Injection Photodetectors. *Nat. Electron.* **2022**, *5*, 281–288. [CrossRef]
107. Peng, L.; Liu, L.; Du, S.; Bodepudi, S.C.; Li, L.; Liu, W.; Lai, R.; Cao, X.; Fang, W.; Liu, Y.; et al. Macroscopic Assembled Graphene Nanofilms Based Room Temperature Ultrafast Mid-Infrared Photodetectors. *InfoMat* **2022**, *4*, e12309. [CrossRef]
108. Peng, M.; Xie, R.; Wang, Z.; Wang, P.; Wang, F.; Ge, H.; Wang, Y.; Zhong, F.; Wu, P.; Ye, J.; et al. Blackbody-Sensitive Room-Temperature Infrared Photodetectors Based on Low-Dimensional Tellurium Grown by Chemical Vapor Deposition. *Sci. Adv.* **2021**, *7*, eabf7358. [CrossRef] [PubMed]
109. Tong, L.; Huang, X.; Wang, P.; Ye, L.; Peng, M.; An, L.; Sun, Q.; Zhang, Y.; Yang, G.; Li, Z.; et al. Stable Mid-Infrared Polarization Imaging Based on Quasi-2D Tellurium at Room Temperature. *Nat. Commun.* **2020**, *11*, 2308. [CrossRef]
110. Ma, W.; Gao, Y.; Shang, L.; Zhou, W.; Yao, N.; Jiang, L.; Qiu, Q.; Li, J.; Shi, Y.; Hu, Z.; et al. Ultrabroadband Tellurium Photoelectric Detector from Visible to Millimeter Wave. *Adv. Sci.* **2022**, *9*, 2103873. [CrossRef]
111. Bullock, J.; Amani, M.; Cho, J.; Chen, Y.-Z.; Ahn, G.H.; Adinolfi, V.; Shrestha, V.R.; Gao, Y.; Crozier, K.B.; Chueh, Y.-L.; et al. Polarization-Resolved Black Phosphorus/Molybdenum Disulfide Mid-Wave Infrared Photodiodes with High Detectivity at Room Temperature. *Nat. Photonics* **2018**, *12*, 601–607. [CrossRef]

112. Wang, H.; Li, Z.; Li, D.; Chen, P.; Pi, L.; Zhou, X.; Zhai, T. Van der Waals Integration Based on Two-Dimensional Materials for High-Performance Infrared Photodetectors. *Adv. Funct. Mater.* **2021**, *31*, 2103106. [CrossRef]
113. Bao, X.; Zhuo, L.; Dong, W.; Guo, J.; Wang, G.; Wang, B.; Wei, Q.; Huang, Z.; Li, J.; Shen, J.; et al. Black Arsenic-Phosphorus Nanosheets for Highly Responsive Photodetection and Dual-Wavelength Ultrafast Pulse Generation at Telecommunication Bands. *ACS Appl. Mater. Interfaces* **2022**, *14*, 52270–52278. [CrossRef] [PubMed]
114. Tamalampudi, S.R.; Villegas, J.E.; Dushaq, G.; Sankar, R.; Paredes, B.; Rasras, M. High-Speed Waveguide-Integrated InSe Photodetector on SiN Photonics for Near-Infrared Applications. *Adv. Photonics Res.* **2023**, *4*, 2300162. [CrossRef]
115. Li, P.; Hao, Q.; Liu, J.; Qi, D.; Gan, H.; Zhu, J.; Liu, F.; Zheng, Z.; Zhang, W. Flexible Photodetectors Based on All-Solution-Processed Cu Electrodes and InSe Nanoflakes with High Stabilities. *Adv. Funct. Mater.* **2022**, *32*, 2108261. [CrossRef]
116. Ahmad, W.; Liu, J.; Jiang, J.; Hao, Q.; Wu, D.; Ke, Y.; Gan, H.; Laxmi, V.; Ouyang, Z.; Ouyang, F.; et al. Strong Interlayer Transition in Few-Layer InSe/$PdSe_2$ van der Waals Heterostructure for Near-Infrared Photodetection. *Adv. Funct. Mater.* **2021**, *31*, 2104143. [CrossRef]
117. Tang, B.; Hou, L.; Sun, M.; Lv, F.; Liao, J.; Ji, W.; Chen, Q. UV-SWIR Broad Range Photodetectors Made from Few-Layer α-In_2Se_3 Nanosheets. *Nanoscale* **2019**, *11*, 12817–12828. [CrossRef]
118. Jia, C.; Wu, S.; Fan, J.; Luo, C.; Fan, M.; Li, M.; He, L.; Yang, Y.; Zhang, H. Ferroelectrically Modulated and Enhanced Photoresponse in a Self-Powered α-In_2Se_3/Si Heterojunction Photodetector. *ACS Nano* **2023**, *17*, 6534–6544. [CrossRef] [PubMed]
119. Guo, H.; Xia, Y.; Yu, Y.; Zhou, R.; Niu, H.; Mao, X.; Wan, L.; Xu, J. High-Speed and Broadband Spectral Photodetectors Based on β-In_2Se_3/Si Heterojunction. *Materi. Sci. Semicon. Proc.* **2022**, *138*, 106304. [CrossRef]
120. Tang, L.; Teng, C.; Luo, Y.; Khan, U.; Pan, H.; Cai, Z.; Zhao, Y.; Liu, B.; Cheng, H.-M. Confined van der Waals Epitaxial Growth of Two-Dimensional Large Single-Crystal In_2Se_3 for Flexible Broadband Photodetectors. *Research* **2019**, *2019*, 2763704. [CrossRef]
121. Li, Q.; Wei, A.; Lu, J.; Tao, L.; Yang, Y.; Luo, D.; Liu, J.; Xiao, Y.; Zhao, Y.; Li, J. Synthesis of Submillimeter-Scale Single Crystal Stannous Sulfide Nanoplates for Visible and Near-Infrared Photodetectors with Ultrahigh Responsivity. *Adv. Electron. Mater.* **2018**, *4*, 1800154. [CrossRef]
122. Kumar, M.; Rani, S.; Vashistha, P.; Pandey, A.; Gupta, G.; Husale, S.; Singh, V.N. Low Bias Operated, Fast Response SnSe Thin Film Vis-NIR Photodetector on Glass substrate Using One-Step Thermal Evaporation Technique. *J. Alloys Compd.* **2021**, *879*, 160370. [CrossRef]
123. Xu, H.; Hao, L.; Liu, H.; Dong, S.; Wu, Y.; Liu, Y.; Cao, B.; Wang, Z.; Ling, C.; Li, S.; et al. Flexible SnSe Photodetectors with Ultrabroad Spectral Response up to 10.6 µm Enabled by Photobolometric Effect. *ACS Appl. Mater. Interfaces* **2020**, *12*, 35250–35258. [CrossRef] [PubMed]
124. Yan, Y.; Abbas, G.; Li, F.; Li, Y.; Zheng, B.; Wang, H.; Liu, F. Self-Driven High Performance Broadband Photodetector Based on SnSe/InSe van der Waals Heterojunction. *Adv. Mater. Interfaces* **2022**, *9*, 2102068. [CrossRef]
125. Chen, J.; Lu, S.; Hu, Y.; Yang, F.; Han, H.; Kong, L.; He, B.; Ruan, S.; Xiang, B. Ultrasensitive Bidirectional Photoresponse $SnSe_2$ Photodetector Integration with Thin-Film Lithium Niobate Photonics. *Adv. Opt. Mater.* **2024**, *12*, 2301543. [CrossRef]
126. Zankat, C.K.; Pataniya, P.M.; Patel, A.; Bhakhar, S.A.; Narayan, S.; Solanki, G.K.; Patel, K.D.; Pathak, V.M.; Sumesh, C.K.; Jha, P.K. Self-Powered Photodetector Based on $SnSe_2$/$MoSe_2$ Heterostructure. *Mater. Today Energy* **2020**, *18*, 100550. [CrossRef]
127. Kim, K.S.; Ji, Y.J.; Kim, K.H.; Choi, S.; Kang, D.-H.; Heo, K.; Cho, S.; Yim, S.; Lee, S.; Park, J.-H.; et al. Ultrasensitive MoS_2 Photodetector by Serial Nano-Bridge Multi-Heterojunction. *Nat. Commun.* **2019**, *10*, 4701. [CrossRef] [PubMed]
128. Huang, Z.; Zhang, T.; Liu, J.; Zhang, L.; Jin, Y.; Wang, J.; Jiang, K.; Fan, S.; Li, Q. Amorphous MoS_2 Photodetector with Ultra-Broadband Response. *ACS Appl. Electron. Mater.* **2019**, *1*, 1314–1321. [CrossRef]
129. Debnath, S.; Meyyappan, M.; Giri, P.K. Printed $MoSe_2$/GaAs Photodetector Enabling Ultrafast and Broadband Photodetection up to 1.5 µm. *ACS Appl. Mater. Interfaces* **2024**, *16*, 9039–9050. [CrossRef]
130. Wang, Z.; Chen, Y.; Wu, P.; Ye, J.; Peng, M.; Yan, Y.; Zhong, F.; He, T.; Wang, Y.; Xu, M.; et al. High-Performance $MoSe_2$ Homojunction Infrared Photodetector. *Infrared Phys. Techn.* **2020**, *106*, 103272. [CrossRef]
131. Jin, H.J.; Park, C.; Byun, H.H.; Park, S.H.; Choi, S.-Y. Electrically Modulated Single/Multicolor High Responsivity 2D $MoTe_2$/MoS_2 Photodetector for Broadband Detection. *ACS Photonics* **2023**, *10*, 3027–3034. [CrossRef]
132. Wu, D.; Guo, J.; Wang, C.; Ren, X.; Chen, Y.; Lin, P.; Zeng, L.; Shi, Z.; Li, X.J.; Shan, C.-X.; et al. Ultrabroadband and High-Detectivity Photodetector Based on WS_2/Ge Heterojunction through Defect Engineering and Interface Passivation. *ACS Nano* **2021**, *15*, 10119–10129. [CrossRef]
133. Hei, J.; Li, X.; Wu, S.; Lin, P.; Shi, Z.; Tian, Y.; Li, X.; Zeng, L.; Yu, X.; Wu, D. Wafer-Scale Patterning Synthesis of Two-Dimensional WSe_2 Layers by Direct Selenization for Highly Sensitive van der Waals Heterojunction Broadband Photodetectors. *ACS Appl. Mater. Interfaces* **2023**, *15*, 12052–12060. [CrossRef]
134. Feng, Y.; Zhang, Y.; Zhang, Y.; Miao, X.; Lin, Y.; Min, T.; Pan, Y. Self-Powered Broadband Photodetectors Based on Large-Scale Continuous Films of Weyl Semimetal WTe_2. *ACS Appl. Opt. Mater.* **2024**, *2*, 333–340. [CrossRef]
135. Zhang, H.; Zhang, X.; Liu, C.; Lee, S.-T.; Jie, J. High-Responsivity, High-Detectivity, Ultrafast Topological Insulator Bi_2Se_3/Silicon Heterostructure Broadband Photodetectors. *ACS Nano* **2016**, *10*, 5113–5122. [CrossRef]
136. Shen, Y.-C.; Lee, C.-Y.; Wang, H.-H.; Kao, M.-H.; Hou, P.-C.; Chen, Y.-Y.; Huang, W.-H.; Shen, C.-H.; Chueh, Y.-L. Embedded Integration of Sb_2Se_3 Film by Low-Temperature Plasma-Assisted Chemical Vapor Reaction with Polycrystalline Si Transistor for High-Performance Flexible Visible-to-Near-Infrared Photodetector. *ACS Nano* **2023**, *17*, 2019–2028. [CrossRef]

137. Yang, J.; Li, J.; Bahrami, A.; Nasiri, N.; Lehmann, S.; Cichocka, M.O.; Mukherjee, S.; Nielsch, K. Wafer-Scale Growth of Sb_2Te_3 Films via Low-Temperature Atomic Layer Deposition for Self-Powered Photodetectors. *ACS Appl. Mater. Interfaces* **2022**, *14*, 54034–54043. [CrossRef]
138. Su, W.; Zhang, S.; Liu, C.; Tian, Q.; Liu, X.; Li, K.; Lv, Y.; Liao, L.; Zou, X. Interlayer Transition Induced Infrared Response in ReS_2/2D Perovskite van der Waals Heterostructure Photodetector. *Nano Lett.* **2022**, *22*, 10192–10199. [CrossRef]
139. Song, Y.; Li, M.; Chen, J.; Du, Y.; Qin, Q.; Du, Z.; Zou, F.; Ma, X.; Li, L.; Li, G. High-Performance Photodetector Based on the $ReSe_2$/$PtSe_2$ van der Waals Heterojunction. *ACS Appl. Electron. Mater.* **2023**, *5*, 2748–2757. [CrossRef]
140. Lu, Y.; Wang, Y.; Xu, C.; Xie, C.; Li, W.; Ding, J.; Zhou, W.; Qin, Z.; Shen, X.; Luo, L.-B. Construction of $PtSe_2$/Ge Heterostructure-Based Short-Wavelength Infrared Photodetector Array for Image Sensing and Optical Communication Applications. *Nanoscale* **2021**, *13*, 7606–7612. [CrossRef]
141. Tong, X.-W.; Lin, Y.-N.; Huang, R.; Zhang, Z.-X.; Fu, C.; Wu, D.; Luo, L.-B.; Li, Z.-J.; Liang, F.-X.; Zhang, W. Direct Tellurization of Pt to Synthesize 2D $PtTe_2$ for High-Performance Broadband Photodetectors and NIR Image Sensors. *ACS Appl. Mater. Interfaces* **2020**, *12*, 53921–53931. [CrossRef] [PubMed]
142. Liu, M.; Wei, J.; Qi, L.; An, J.; Liu, X.; Li, Y.; Shi, Z.; Li, D.; Novoselov, K.S.; Qiu, C.-W.; et al. Photogating-Assisted Tunneling Boosts the Responsivity and Speed of Heterogeneous WSe_2/Ta_2NiSe_5 Photodetectors. *Nat. Commun.* **2024**, *15*, 141. [CrossRef] [PubMed]
143. Jiao, H.; Wang, X.; Chen, Y.; Guo, S.; Wu, S.; Song, C.; Huang, S.; Huang, X.; Tai, X.; Lin, T.; et al. HgCdTe/Black Phosphorus van der Waals Heterojunction for High-Performance Polarization-Sensitive Midwave Infrared Photodetector. *Sci. Adv.* **2022**, *8*, eabn1811. [CrossRef] [PubMed]
144. Zhu, C.-Y.; Zhang, Z.; Qin, J.-K.; Wang, Z.; Wang, C.; Miao, P.; Liu, Y.; Huang, P.-Y.; Zhang, Y.; Xu, K.; et al. Two-Dimensional Semiconducting SnP_2Se_6 with Giant Second-Harmonic-Generation for Monolithic on-Chip Electronic-Photonic Integration. *Nat. Commun.* **2023**, *14*, 2521. [CrossRef]
145. Palaferri, D.; Todorov, Y.; Bigioli, A.; Mottaghizadeh, A.; Gacemi, D.; Calabrese, A.; Vasanelli, A.; Li, L.; Davies, A.G.; Linfield, E.H.; et al. Room-Temperature Nine-µm-Wavelength Photodetectors and GHz-Frequency Heterodyne Receivers. *Nature* **2018**, *556*, 85–88. [CrossRef] [PubMed]
146. Dey, A.W.; Svensson, J.; Borg, B.M.; Ek, M.; Wernersson, L.-E. Single InAs/GaSb Nanowire Low-Power CMOS Inverter. *Nano Lett.* **2012**, *12*, 5593–5597. [CrossRef] [PubMed]
147. Tan, H.; Fan, C.; Ma, L.; Zhang, X.; Fan, P.; Yang, Y.; Hu, W.; Zhou, H.; Zhuang, X.; Zhu, X.; et al. Single-Crystalline InGaAs Nanowires for Room-Temperature High-Performance Near-Infrared Photodetectors. *Nano-Micro Lett.* **2016**, *8*, 29–35. [CrossRef] [PubMed]
148. Yin, Y.; Guo, Y.; Liu, D.; Miao, C.; Liu, F.; Zhuang, X.; Tan, Y.; Chen, F.; Yang, Z.-x. Substrate-Free Chemical Vapor Deposition of Large-Scale III–V Nanowires for High-Performance Transistors and Broad-Spectrum Photodetectors. *Adv. Opt. Mater.* **2022**, *10*, 2102291. [CrossRef]
149. Zhang, K.; Ren, Z.; Cao, H.; Li, L.; Wang, Y.; Zhang, W.; Li, Y.; Yang, H.; Meng, Y.; Ho, J.C.; et al. Near-Infrared Polarimetric Image Sensors Based on Ordered Sulfur-Passivation GaSb Nanowire Arrays. *ACS Nano* **2022**, *16*, 8128–8140. [CrossRef]
150. Wang, J.; Jiang, C.; Li, W.; Xiao, X. Anisotropic Low-Dimensional Materials for Polarization-Sensitive Photodetectors: From Materials to Devices. *Adv. Opt. Mater.* **2022**, *10*, 2102436. [CrossRef]
151. Mauthe, S.; Baumgartner, Y.; Sousa, M.; Ding, Q.; Rossell, M.D.; Schenk, A.; Czornomaz, L.; Moselund, K.E. High-Speed III–V Nanowire Photodetector Monolithically Integrated on Si. *Nat. Commun.* **2020**, *11*, 4565. [CrossRef]
152. Wang, X.; Pan, D.; Han, Y.; Sun, M.; Zhao, J.; Chen, Q. Vis-IR Wide-Spectrum Photodetector at Room Temperature Based on p-n Junction-Type $GaAs_{1-x}Sb_x$/InAs Core-Shell Nanowire. *ACS Appl. Mater. Interfaces* **2019**, *11*, 38973–38981. [CrossRef]
153. Lähnemann, J.; Ajay, A.; Den Hertog, M.I.; Monroy, E. Near-Infrared Intersubband Photodetection in GaN/AlN Nanowires. *Nano Lett.* **2017**, *17*, 6954–6960. [CrossRef]
154. Li, X.; Zhang, J.; Yue, C.; Tang, X.; Gao, Z.; Jiang, Y.; Du, C.; Deng, Z.; Jia, H.; Wang, W.; et al. High Performance Visible-SWIR Flexible Photodetector Based on Large-Area InGaAs/InP PIN Structure. *Sci. Rep.* **2022**, *12*, 7681. [CrossRef]
155. Zhang, H.; Wang, W.; Yip, S.; Li, D.; Li, F.; Lan, C.; Wang, F.; Liu, C.; Ho, J.C. Enhanced Performance of Near-Infrared Photodetectors Based on InGaAs Nanowires Enabled by a Two-Step Growth Method. *J. Mater. Chem. C* **2020**, *8*, 17025–17033. [CrossRef]
156. Zhang, S.; Jiao, H.; Wang, X.; Chen, Y.; Wang, H.; Zhu, L.; Jiang, W.; Liu, J.; Sun, L.; Lin, T.; et al. Highly Sensitive InSb Nanosheets Infrared Photodetector Passivated by Ferroelectric Polymer. *Adv. Funct. Mater.* **2020**, *30*, 2006156. [CrossRef]
157. Li, Z.; Azimi, Z.; Li, Z.; Yu, Y.; Huang, L.; Jin, W.; Tan, H.H.; Jagadish, C.; Wong-Leung, J.; Fu, L. InAs Nanowire Arrays for Room-Temperature Ultra-Broadband Infrared Photodetection. *Nanoscale* **2023**, *15*, 10033–10041. [CrossRef]
158. Jung, B.K.; Yoo, H.; Seo, B.; Choi, H.J.; Choi, Y.K.; Kim, T.H.; Oh, N.; Kim, S.Y.; Kim, S.; Lee, Y.; et al. High-Affinity Ligand-Enhanced Passivation of Group III–V Colloidal Quantum Dots for Sensitive Near-Infrared Photodetection. *ACS Energy Lett.* **2024**, *9*, 504–512. [CrossRef]
159. Mano, T.; Ohtake, A.; Kawazu, T.; Miyazaki, H.T.; Sakuma, Y. Low Dark Current Operation in InAs/GaAs(111)A Infrared Photodetectors: Role of Misfit Dislocations at the Interface. *ACS Appl. Mater. Interfaces* **2023**, *15*, 29636–29642. [CrossRef]
160. Jia, B.W.; Tan, K.H.; Loke, W.K.; Wicaksono, S.; Lee, K.H.; Yoon, S.F. Monolithic Integration of InSb Photodetector on Silicon for Mid-Infrared Silicon Photonics. *ACS Photonics* **2018**, *5*, 1512–1520. [CrossRef]

161. Liu, F.; Zhuang, X.; Wang, M.; Qi, D.; Dong, S.; Yip, S.; Yin, Y.; Zhang, J.; Sa, Z.; Song, K.; et al. Lattice-Mismatch-Free Construction of III–V/Chalcogenide Core-Shell Heterostructure Nanowires. *Nat. Commun.* **2023**, *14*, 7480. [CrossRef] [PubMed]
162. Li, D.; Lan, C.; Manikandan, A.; Yip, S.; Zhou, Z.; Liang, X.; Shu, L.; Chueh, Y.-L.; Han, N.; Ho, J.C. Ultra-Fast Photodetectors Based on High-Mobility Indium Gallium Antimonide Nanowires. *Nat. Commun.* **2019**, *10*, 1664. [CrossRef] [PubMed]
163. Shafir, I.; Snapi, N.; Cohen-Elias, D.; Glozman, A.; Klin, O.; Weiss, E.; Westreich, O.; Sicron, N.; Katz, M. High Responsivity InGaAsSb p-n Photodetector for Extended SWIR Detection. *Appl. Phys. Lett.* **2021**, *118*, 063503. [CrossRef]
164. Li, D.; Yip, S.; Li, F.; Zhang, H.; Meng, Y.; Bu, X.; Kang, X.; Lan, C.; Liu, C.; Ho, J.C. Flexible Near-Infrared InGaSb Nanowire Array Detectors with Ultrafast Photoconductive Response Below 20 μs. *Adv. Opt. Mater.* **2020**, *8*, 2001201. [CrossRef]
165. Pokharel, R.; Ramaswamy, P.; Devkota, S.; Parakh, M.; Dawkins, K.; Penn, A.; Cabral, M.; Reynolds, L.; Iyer, S. Epitaxial High-Yield Intrinsic and Te-Doped Dilute Nitride GaAsSbN Nanowire Heterostructure and Ensemble Photodetector Application. *ACS Appl. Electron. Mater.* **2020**, *2*, 2730–2738. [CrossRef]
166. Ren, Z.; Wang, P.; Zhang, K.; Ran, W.; Yang, J.; Liu, Y.Y.; Lou, Z.; Shen, G.; Wei, Z. Short-Wave Near-Infrared Polarization Sensitive Photodetector Based on GaSb Nanowire. *IEEE Electron Device Lett.* **2021**, *42*, 549–552. [CrossRef]
167. Zhou, C.; Zhang, X.-T.; Zheng, K.; Chen, P.-P.; Lu, W.; Zou, J. Self-Assembly Growth of In-Rich InGaAs Core-Shell Structured Nanowires with Remarkable Near-Infrared Photoresponsivity. *Nano Lett.* **2017**, *17*, 7824–7830. [CrossRef] [PubMed]
168. Nalamati, S.; Devkota, S.; Li, J.; Lavelle, R.; Huet, B.; Snyder, D.; Penn, A.; Garcia, R.; Reynolds, L., Jr.; Iyer, S. Hybrid GaAsSb/GaAs Heterostructure Core-Shell Nanowire/Graphene and Photodetector Applications. *ACS Appl. Electron. Mater.* **2020**, *2*, 3109–3120. [CrossRef]
169. Li, L.; Liu, X.; Li, Y.; Xu, Z.; Wu, Z.; Han, S.; Tao, K.; Hong, M.; Luo, J.; Sun, Z. Two-Dimensional Hybrid Perovskite-Type Ferroelectric for Highly Polarization-Sensitive Shortwave Photodetection. *J. Am. Chem. Soc.* **2019**, *141*, 2623–2629. [CrossRef]
170. Ruppel, C.C.W. Acoustic Wave Filter Technology-A Review. *IEEE Trans. Ultrason. Ferroelectr. Freq. Control* **2017**, *64*, 1390–1400. [CrossRef]
171. Davis, M.; Damjanovic, D.; Setter, N. Pyroelectric Properties of $(1-x)Pb(Mg_{1/3}Nb_{2/3})O_3$-$xPbTiO_3$ and $(1-x)Pb(Zn_{1/3}Nb_{2/3})O_3$-$xPbTiO_3$ Single Crystals Measured Using a Dynamic Method. *J. Appl. Phys.* **2004**, *96*, 2811–2815. [CrossRef]
172. Lian, J.; Tao, J.; Chai, X.; Zhang, Y.; Jiang, A. Effects of Atmosphere, Metal Films, Temperatures and Holding Time on the Surface Topography and Electrical Conductivity of $LiNbO_3$ Single Crystals. *Ceram. Int.* **2019**, *45*, 9736–9753. [CrossRef]
173. Tang, L.; Han, S.; Ma, Y.; Liu, Y.; Hua, L.; Xu, H.; Guo, W.; Wang, B.; Sun, Z.; Luo, J. Giant Near-Room-Temperature Pyroelectric Figures-of-Merit Originating from Unusual Dielectric Bistability of Two-Dimensional Perovskite Ferroelectric Crystals. *Chem. Eng. Sci.* **2022**, *34*, 8898–8904. [CrossRef]
174. Tian, M.; Liu, X.; Gong, A.; Zhang, S.; Wang, G.; Han, P.; Li, Y.; Lou, X.; Hao, X. Efficient Ultraviolet-Visible-Near Infrared Self-Powered Photodetector Based on Hexagonal $YMnO_3$-Based Ferroelectric Thin Film by Multiscale Polarity Structure Optimization. *Chem. Eng. J.* **2023**, *452*, 139040. [CrossRef]
175. Tiwari, R.P.; Hashmi, S.Z.H.; Sharma, R.; Khan, S.A.; Birajdar, B. Synthesis of Highly Pure and Dense $0.9(KNbO_3)$-$0.1(BaNi_{1/2}Nb_{1/2}O_{3-\delta})$ Ceramic with Superior Magnetic Properties. *J. Am. Ceram. Soc.* **2019**, *102*, 4659–4669. [CrossRef]
176. Huangfu, G.; Xiao, H.; Guan, L.; Zhong, H.; Hu, C.; Shi, Z.; Guo, Y. Visible or Near-Infrared Light Self-Powered Photodetectors Based on Transparent Ferroelectric Ceramics. *ACS Appl. Mater. Interfaces* **2020**, *12*, 33950–33959. [CrossRef]
177. Gopalan, K.K.; Janner, D.; Nanot, S.; Parret, R.; Lundeberg, M.B.; Koppens, F.H.L.; Pruneri, V. Mid-Infrared Pyroresistive Graphene Detector on $LiNbO_3$. *Adv. Opt. Mater.* **2017**, *5*, 1600723. [CrossRef]
178. Guan, H.; Hong, J.; Wang, X.; Ming, J.; Zhang, Z.; Liang, A.; Han, X.; Dong, J.; Qiu, W.; Chen, Z.; et al. Broadband, High-Sensitivity Graphene Photodetector Based on Ferroelectric Polarization of Lithium Niobate. *Adv. Opt. Mater.* **2021**, *9*, 2100245. [CrossRef]
179. Wang, L.; Chen, C.; He, X.; Yao, K.; Yi, Z. Non-Stoichiometric BZT-BCT Ferroelectrics with Visible/Near-Infrared Photoresponse for Broadband Photodetection. *J. Am. Ceram. Soc.* **2023**, *106*, 389–398. [CrossRef]
180. Gong, A.; Zhang, S.; Li, Y.; Han, P.; Lu, C.; Sun, N.; Zhao, Y.; Xing, L.; Zhang, L.; Hao, X. Broadband, High-Sensitivity Self-Powered Ferroelectric $LuMnO_3$-Based Photodetector with Large Photocurrent Output. *Ceram. Int.* **2023**, *49*, 12462–12468. [CrossRef]
181. Wang, J.; Ma, J.; Yang, Y.; Chen, M.; Zhang, J.; Ma, J.; Nan, C.-W. Ferroelectric Photodetector with High Current on-off Ratio (~1×10^4%) in Self-Assembled Topological Nanoislands. *ACS Appl. Electron. Mater.* **2019**, *1*, 862–868. [CrossRef]
182. Yao, Y.; Liang, Y.; Shrotriya, V.; Xiao, S.; Yu, L.; Yang, Y. Plastic Near-Infrared Photodetectors Utilizing Low Band Gap Polymer. *Adv. Mater.* **2007**, *19*, 3979–3983. [CrossRef]
183. Gong, X.; Tong, M.; Xia, Y.; Cai, W.; Moon, J.S.; Cao, Y.; Yu, G.; Shieh, C.-L.; Nilsson, B.; Heeger, A.J. High-Detectivity Polymer Photodetectors with Spectral Response from 300 nm to 1450 nm. *Science* **2009**, *325*, 1665–1667. [CrossRef] [PubMed]
184. Zheng, L.; Zhu, T.; Xu, W.; Liu, L.; Zheng, J.; Gong, X.; Wudl, F. Solution-Processed Broadband Polymer Photodetectors with a Spectral Response of up to 2.5 μm by a Low Bandgap Donor-Acceptor Conjugated Copolymer. *J. Mater. Chem. C* **2018**, *6*, 3634–3641. [CrossRef]
185. Gielen, S.; Kaiser, C.; Verstraeten, F.; Kublitski, J.; Benduhn, J.; Spoltore, D.; Verstappen, P.; Maes, W.; Meredith, P.; Armin, A.; et al. Intrinsic Detectivity Limits of Organic Near-Infrared Photodetectors. *Adv. Mater.* **2020**, *32*, 2003818. [CrossRef]
186. Xiang, H.; Xin, C.; Hu, Z.; Aigouy, L.; Chen, Z.; Yuan, X. Long-Term Stable Near-Infrared-Short-Wave-Infrared Photodetector Driven by the Photothermal Effect of Polypyrrole Nanostructures. *ACS Appl. Mater. Interfaces* **2021**, *13*, 45957–45965. [CrossRef] [PubMed]

187. Gibert-Roca, M.; Molet, P.; Mihi, A.; Campoy-Quiles, M. Near Infrared Organic Photodetectors Based on Enhanced Charge Transfer StateAbsorption by Photonic Architectures. *J. Mater. Chem. C* **2020**, *8*, 9688–9696. [CrossRef]
188. Li, Q.; Ran, Y.; Shi, W.; Qin, M.; Sun, Y.; Kuang, J.; Wang, H.; Chen, H.; Guo, Y.; Liu, Y. High-Performance Near-Infrared Polymeric Phototransistors Realized by Combining Cross-Linked Polymeric Semiconductors and Bulk Heterojunction Bilayer structures. *Appl. Mater. Today* **2021**, *22*, 100899. [CrossRef]
189. Han, T.; Li, X.; Zhang, J.; Tang, W.; Jiang, S.; Pan, C.; Qian, Y.; Ding, S.; Chen, Y.; Jiang, C. Controlling Electron Transfer in a Lateral Near-Infrared Polymer Photodetector by Adding Higher-LUMO-Level Acceptors: A Pathway to Reduce Dark Current. *J. Mater. Chem. C* **2024**, *12*, 5203–5212. [CrossRef]
190. Wang, C.; Chen, X.; Chen, F.; Shao, J. Organic Photodetectors Based on Copper Phthalocyanine Films Prepared by a Multiple Drop Casting Method. *Org. Electron.* **2019**, *66*, 183–187. [CrossRef]
191. Zou, T.; Wang, X.; Ju, H.; Wu, Q.; Guo, T.; Wu, W.; Wang, H. Crystal Structure Tuning in Organic Nanomaterials for Fast Response and High Sensitivity Visible-NIR Photo-Detector. *J. Mater. Chem. C* **2018**, *6*, 1495–1503. [CrossRef]
192. Choi, M.-S.; Lee, S.; Kim, H.J.; Kim, J.-J. Inverted Near-Infrared Organic Photodetector with Oriented Lead (II) Phthalocyanine Molecules via Substrate Heating. *Org. Electron.* **2018**, *61*, 164–169. [CrossRef]
193. Shan, H.; Wang, Y.; Li, C.; Hu, Q.; Sun, X.; Dong, L.; Feng, Y.; Ye, W.; Xu, J.; Xu, Z.-X. Solution-Processed Near-Infrared Phototransistor Based on Ultrathin Nanocrystals of Octamethyl Substituted Zinc(II) Phthalocyanine. *Org. Electron.* **2018**, *58*, 197–201. [CrossRef]
194. Kabir, S.; Takayashiki, Y.; Ohno, A.; Hanna, J.-I.; Iino, H. Near-Infrared Organic Photodetectors with a Soluble Alkoxy-Phthalocyanine Derivative. *Opt. Mater.* **2022**, *126*, 112209. [CrossRef]
195. Raveendra Kiran, M.; Ulla, H.; Satyanarayan, M.N.; Umesh, G. Optoelectronic Properties of Hybrid Diodes Based on Vanadyl-Phthalocyanine and Zinc Oxide Nanorods Thin Films. *Opt. Mater.* **2019**, *96*, 109348. [CrossRef]
196. Huang, F.; Peng, Y.; Liu, G. Toward Ultrahigh Sensitivity and UV-Vis-NIR Broadband Response of Organolead Halide Perovskite/Tin-Phthalocyanine Heterostructured Photodetectors. *J. Mater. Chem. C* **2019**, *123*, 11073–11080. [CrossRef]
197. Wang, M.; Li, Y.-Z.; Chen, H.-C.; Liu, C.-W.; Chen, Y.-S.; Lo, Y.-C.; Tsao, C.-S.; Huang, Y.-C.; Liu, S.-W.; Wong, K.-T.; et al. Unveiling the Underlying Mechanism of Record-High Efficiency Organic Near-Infrared Photodetector Harnessing a Single-Component Photoactive Layer. *Mater. Horiz.* **2020**, *7*, 1171–1179. [CrossRef]
198. Li, N.; Eedugurala, N.; Azoulay, J.D.; Ng, T.N. A Filterless Organic Photodetector Electrically Switchable between Visible and Infrared Detection. *Cell Rep. Phys. Sci.* **2022**, *3*, 100711. [CrossRef]
199. Huang, J.; Lee, J.; Vollbrecht, J.; Brus, V.V.; Dixon, A.L.; Cao, D.X.; Zhu, Z.; Du, Z.; Wang, H.; Cho, K.; et al. A High-Performance Solution-Processed Organic Photodetector for Near-Infrared Sensing. *Adv. Mater.* **2020**, *32*, 1906027. [CrossRef]
200. Bhat, G.; Kielar, M.; Sah, P.; Pandey, A.K.; Sonar, P. Solution-Processed Ternary Organic Photodetectors with Ambipolar Small-Bandgap Polymer for Near-Infrared Sensing. *Adv. Electron. Mater.* **2024**, *10*, 2300583. [CrossRef]
201. Jacoutot, P.; Scaccabarozzi, A.D.; Zhang, T.; Qiao, Z.; Aniés, F.; Neophytou, M.; Bristow, H.; Kumar, R.; Moser, M.; Nega, A.D.; et al. Infrared Organic Photodetectors Employing Ultralow Bandgap Polymer and Non-Fullerene Acceptors for Biometric Monitoring. *Small* **2022**, *18*, 2200580. [CrossRef]
202. Xing, S.; Kublitski, J.; Hänisch, C.; Winkler, L.C.; Li, T.-Y.; Kleemann, H.; Benduhn, J.; Leo, K. Photomultiplication-Type Organic Photodetectors for Near-Infrared Sensing with High and Bias-Independent Specific Detectivity. *Adv. Sci.* **2022**, *9*, 2105113. [CrossRef]
203. Wu, Z.; Yao, W.; London, A.E.; Azoulay, J.D.; Ng, T.N. Elucidating the Detectivity Limits in Shortwave Infrared Organic Photodiodes. *Adv. Funct. Mater.* **2018**, *28*, 1800391. [CrossRef]
204. Gréboval, C.; Chu, A.; Goubet, N.; Livache, C.; Ithurria, S.; Lhuillier, E. Mercury Chalcogenide Quantum Dots: Material Perspective for Device Integration. *Chem. Rev.* **2021**, *121*, 3627–3700. [CrossRef]
205. Lawson, W.D.; Nielsen, S.; Putley, E.H.; Young, A.S. Preparation and properties of HgTe and mixed crystals of HgTe-CdTe. *J. Phys. Chem. Solids* **1959**, *9*, 325–329. [CrossRef]
206. Wang, Y.; Yang, D.; Ma, D.; Kim, D.H.; Ahamad, T.; Alshehri, S.M.; Vadim, A. Organic-Inorganic Hybrid Sn-Based Perovskite Photodetectors with High External Quantum Efficiencies and Wide Spectral Responses from 300 to 1000 nm. *Sci. China Mater.* **2019**, *62*, 790–796. [CrossRef]
207. Cryer, M.E.; Halpert, J.E. 300 nm Spectral Resolution in the Mid-Infrared with Robust, High Responsivity Flexible Colloidal Quantum Dot Devices at Room Temperature. *ACS Photonics* **2018**, *5*, 3009–3015. [CrossRef]
208. Chu, A.; Gréboval, C.; Goubet, N.; Martinez, B.; Livache, C.; Qu, J.; Rastogi, P.; Bresciani, F.A.; Prado, Y.; Suffit, S.; et al. Near Unity Absorption in Nanocrystal Based Short Wave Infrared Photodetectors Using Guided Mode Resonators. *ACS Photonics* **2019**, *6*, 2553–2561. [CrossRef]
209. Zhang, S.; Bi, C.; Tan, Y.; Luo, Y.; Liu, Y.; Cao, J.; Chen, M.; Hao, Q.; Tang, X. Direct Optical Lithography Enabled Multispectral Colloidal Quantum-Dot Imagers from Ultraviolet to Short-Wave Infrared. *ACS Nano* **2022**, *16*, 18822–18829. [CrossRef] [PubMed]
210. Zhu, B.; Chen, M.; Zhu, Q.; Zhou, G.; Abdelazim, N.M.; Zhou, W.; Kershaw, S.V.; Rogach, A.L.; Zhao, N.; Tsang, H.K. Integrated Plasmonic Infrared Photodetector Based on Colloidal HgTe Quantum Dots. *Adv. Mater. Technol.* **2019**, *4*, 1900354. [CrossRef]
211. Chen, M.; Lan, X.; Tang, X.; Wang, Y.; Hudson, M.H.; Talapin, D.V.; Guyot-Sionnest, P. High Carrier Mobility in HgTe Quantum Dot Solids Improves Mid-IR Photodetectors. *ACS Photonics* **2019**, *6*, 2358–2365. [CrossRef]

212. Chu, A.; Gréboval, C.; Prado, Y.; Majjad, H.; Delerue, C.; Dayen, J.-F.; Vincent, G.; Lhuillier, E. Infrared photoconduction at the diffusion length limit in HgTe nanocrystal arrays. *Nat. Commun.* **2021**, *12*, 1794. [CrossRef]
213. Dang, T.H.; Abadie, C.; Khalili, A.; Gréboval, C.; Zhang, H.; Prado, Y.; Xu, X.Z.; Gacemi, D.; Descamps-Mandine, A.; Ithurria, S.; et al. Broadband Enhancement of Mid-Wave Infrared Absorption in a Multi-Resonant Nanocrystal-Based Device. *Adv. Opt. Mater.* **2022**, *10*, 2200297. [CrossRef]
214. Dang, T.H.; Khalili, A.; Abadie, C.; Gréboval, C.; Cavallo, M.; Zhang, H.; Bossavit, E.; Utterback, J.K.; Dandeu, E.; Prado, Y.; et al. Nanocrystal-Based Active Photonics Device through Spatial Design of Light-Matter Coupling. *ACS Photonics* **2022**, *9*, 2528–2535. [CrossRef]
215. Dong, Y.; Chen, M.; Yiu, W.K.; Zhu, Q.; Zhou, G.; Kershaw, S.V.; Ke, N.; Wong, C.P.; Rogach, A.L.; Zhao, N. Solution Processed Hybrid Polymer: HgTe Quantum Dot Phototransistor with High Sensitivity and Fast Infrared Response up to 2400 nm at Room Temperature. *Adv. Sci.* **2020**, *7*, 2000068. [CrossRef] [PubMed]
216. Grotevent, M.J.; Hail, C.U.; Yakunin, S.; Bachmann, D.; Calame, M.; Poulikakos, D.; Kovalenko, M.V.; Shorubalko, I. Colloidal HgTe Quantum Dot/Graphene Phototransistor with a Spectral Sensitivity Beyond 3 µm. *Adv. Sci.* **2021**, *8*, 2003360. [CrossRef] [PubMed]
217. Gréboval, C.; Dabard, C.; Konstantinov, N.; Cavallo, M.; Chee, S.-S.; Chu, A.; Dang, T.H.; Khalili, A.; Izquierdo, E.; Prado, Y.; et al. Split-Gate Photodiode Based on Graphene/HgTe Heterostructures with a Few Nanosecond Photoresponse. *ACS Appl. Electron. Mater.* **2021**, *3*, 4681–4688. [CrossRef]
218. Tang, X.; Ackerman, M.M.; Guyot-Sionnest, P. Thermal Imaging with Plasmon Resonance Enhanced HgTe Colloidal Quantum Dot Photovoltaic Devices. *ACS Nano* **2018**, *12*, 7362–7370. [CrossRef]
219. Martinez, B.; Ramade, J.; Livache, C.; Goubet, N.; Chu, A.; Gréboval, C.; Qu, J.; Watkins, W.L.; Becerra, L.; Dandeu, E.; et al. HgTe Nanocrystal Inks for Extended Short-Wave Infrared Detection. *Adv. Opt. Mater.* **2019**, *7*, 1900348. [CrossRef]
220. Tang, X.; Ackerman, M.M.; Shen, G.; Guyot-Sionnest, P. Towards Infrared Electronic Eyes: Flexible Colloidal Quantum Dot Photovoltaic Detectors Enhanced by Resonant Cavity. *Small* **2019**, *15*, 1804920. [CrossRef]
221. Tang, X.; Ackerman, M.M.; Guyot-Sionnest, P. Acquisition of Hyperspectral Data with Colloidal Quantum Dots. *Laser Photonics Rev.* **2019**, *13*, 1900165. [CrossRef]
222. Gréboval, C.; Izquierdo, E.; Abadie, C.; Khalili, A.; Cavallo, M.; Chu, A.; Dang, T.H.; Zhang, H.; Lafosse, X.; Rosticher, M.; et al. HgTe Nanocrystal-Based Photodiode for Extended Short-Wave Infrared Sensing with Optimized Electron Extraction and Injection. *ACS Appl. Nano Mater.* **2022**, *5*, 8602–8611. [CrossRef]
223. Rastogi, P.; Izquierdo, E.; Gréboval, C.; Cavallo, M.; Chu, A.; Dang, T.H.; Khalili, A.; Abadie, C.; Alchaar, R.; Pierini, S.; et al. Extended Short-Wave Photodiode Based on CdSe/HgTe/Ag_2Te Stack with High Internal Efficiency. *J. Phys. Chem. C* **2022**, *126*, 13720–13728. [CrossRef]
224. Chen, M.; Hao, Q.; Luo, Y.; Tang, X. Mid-Infrared Intraband Photodetector via High Carrier Mobility HgSe Colloidal Quantum Dots. *ACS Nano* **2022**, *16*, 11027–11035. [CrossRef]
225. Khalili, A.; Weis, M.; Mizrahi, S.G.; Chu, A.; Dang, T.H.; Abadie, C.; Gréboval, C.; Dabard, C.; Prado, Y.; Xu, X.Z.; et al. Guided-Mode Resonator Coupled with Nanocrystal Intraband Absorption. *ACS Photonics* **2022**, *9*, 985–993. [CrossRef]
226. Alwadai, N.; Haque, M.A.; Mitra, S.; Flemban, T.; Pak, Y.; Wu, T.; Roqan, I. High-Performance Ultraviolet-to-Infrared Broadband Perovskite Photodetectors Achieved via Inter-/Intraband Transitions. *ACS Appl. Mater. Interfaces* **2017**, *9*, 37832–37838. [CrossRef]
227. Cao, F.; Liao, Q.; Deng, K.; Chen, L.; Li, L.; Zhang, Y. Novel Perovskite/TiO_2/Si Trilayer Heterojunctions for High-Performance Self-Powered Ultraviolet-Visible-Near Infrared (UV-Vis-NIR) Photodetectors. *Nano Res.* **2018**, *11*, 1722–1730. [CrossRef]
228. Sun, H.; Tian, W.; Cao, F.; Xiong, J.; Li, L. Ultrahigh-Performance Self-Powered Flexible Double-Twisted Fibrous Broadband Perovskite Photodetector. *Adv. Mater.* **2018**, *30*, 1706986. [CrossRef]
229. Zhu, T.; Yang, Y.; Zheng, L.; Liu, L.; Becker, M.L.; Gong, X. Solution-Processed Flexible Broadband Photodetectors with Solution-Processed Transparent Polymeric Electrode. *Adv. Funct. Mater.* **2020**, *30*, 1909487. [CrossRef]
230. Guo, R.; Bao, C.; Gao, F.; Tian, J. Double Active Layers Constructed with Halide Perovskite and Quantum Dots for Broadband Photodetection. *Adv. Opt. Mater.* **2020**, *8*, 2000557. [CrossRef]
231. García de Arquer, F.P.; Gong, X.; Sabatini, R.P.; Liu, M.; Kim, G.-H.; Sutherland, B.R.; Voznyy, O.; Xu, J.; Pang, Y.; Hoogland, S.; et al. Field-Emission from Quantum-Dot-in-Perovskite Solids. *Nat. Commun.* **2017**, *8*, 14757. [CrossRef] [PubMed]
232. Shen, L.; Lin, Y.; Bao, C.; Bai, Y.; Deng, Y.; Wang, M.; Li, T.; Lu, Y.; Gruverman, A.; Li, W.; et al. Integration of Perovskite and Polymer Photoactive Layers to Produce Ultrafast Response, Ultraviolet-to-Near-Infrared, Sensitive Photodetectors. *Mater. Horiz.* **2017**, *4*, 242–248. [CrossRef]
233. Zhang, Y.; Liu, Y.; Yang, Z.; Liu, S. High-Quality Perovskite $MAPbI_3$ Single Crystals for Broad-Spectrum and Rapid Response Integrate Photodetector. *J. Energy Chem.* **2018**, *27*, 722–727. [CrossRef]
234. Liang, F.-X.; Liang, L.; Zhao, X.-Y.; Luo, L.-B.; Liu, Y.-H.; Tong, X.-W.; Zhang, Z.-X.; Huang, J.C.A. A Sensitive Broadband (UV-vis-NIR) Perovskite Photodetector Using Topological Insulator as Electrodes. *Adv. Opt. Mater.* **2019**, *7*, 1801392. [CrossRef]
235. Kang, D.-H.; Pae, S.R.; Shim, J.; Yoo, G.; Jeon, J.; Leem, J.W.; Yu, J.S.; Lee, S.; Shin, B.; Park, J.-H. An Ultrahigh-Performance Photodetector Based on a Perovskite-Transition-Metal-Dichalcogenide Hybrid Structure. *Adv. Mater.* **2016**, *28*, 7799–7806. [CrossRef] [PubMed]
236. Mei, L.; Huang, R.; Shen, C.; Hu, J.; Wang, P.; Xu, Z.; Huang, Z.; Zhu, L. Hybrid Halide Perovskite-Based Near-Infrared Photodetectors and Imaging Arrays. *Adv. Opt. Mater.* **2022**, *10*, 2102656. [CrossRef]

237. Ka, I.; Gerlein, L.F.; Asuo, I.M.; Nechache, R.; Cloutier, S.G. An Ultra-Broadband Perovskite-PbS Quantum Dot Sensitized Carbon Nanotube Photodetector. *Nanoscale* **2018**, *10*, 9044–9052. [CrossRef] [PubMed]
238. Asuo, I.M.; Banerjee, D.; Pignolet, A.; Nechache, R.; Cloutier, S.G. Perovskite/Silicon-Nanowire-Based Hybrid Heterojunctions for Fast and Broadband Photodetectors. *Phys. Status. Solidi-Rapid Res. Lett.* **2021**, *15*, 2000537. [CrossRef]
239. Waleed, A.; Tavakoli, M.M.; Gu, L.; Wang, Z.; Zhang, D.; Manikandan, A.; Zhang, Q.; Zhang, R.; Chueh, Y.-L.; Fan, Z. Lead-Free Perovskite Nanowire Array Photodetectors with Drastically Improved Stability in Nanoengineering Templates. *Nano Lett.* **2017**, *17*, 523–530. [CrossRef]
240. Liu, C.-K.; Tai, Q.; Wang, N.; Tang, G.; Hu, Z.; Yan, F. Lead-Free Perovskite/Organic Semiconductor Vertical Heterojunction for Highly Sensitive Photodetectors. *ACS Appl. Mater. Interfaces* **2020**, *12*, 18769–18776. [CrossRef]
241. Liu, H.; Zhu, H.L.; Wang, Z.; Wu, X.; Huang, Z.; Huqe, M.R.; Zapien, J.A.; Lu, X.; Choy, W.C.H. Double-Side Crystallization Tuning to Achieve over 1 µm Thick and Well-Aligned Block-Like Narrow-Bandgap Perovskites for High-Efficiency Near-Infrared Photodetectors. *Adv. Funct. Mater.* **2021**, *31*, 2010532. [CrossRef]
242. Wang, W.; Zhao, D.; Zhang, F.; Li, L.; Du, M.; Wang, C.; Yu, Y.; Huang, Q.; Zhang, M.; Li, L.; et al. Highly Sensitive Low-Bandgap Perovskite Photodetectors with Response from Ultraviolet to the Near-Infrared Region. *Adv. Funct. Mater.* **2017**, *27*, 1703953. [CrossRef]
243. Xu, X.; Chueh, C.-C.; Jing, P.; Yang, Z.; Shi, X.; Zhao, T.; Lin, L.Y.; Jen, A.K.Y. High-Performance Near-IR Photodetector Using Low-Bandgap $MA_{0.5}FA_{0.5}Pb_{0.5}Sn_{0.5}I_3$ Perovskite. *Adv. Funct. Mater.* **2017**, *27*, 1701053. [CrossRef]
244. Zhu, H.L.; Lin, H.; Song, Z.; Wang, Z.; Ye, F.; Zhang, H.; Yin, W.-J.; Yan, Y.; Choy, W.C.H. Achieving High-Quality Sn-Pb Perovskite Films on Complementary Metal-Oxide-Semiconductor-Compatible Metal/Silicon Substrates for Efficient Imaging Array. *ACS Nano* **2019**, *13*, 11800–11808. [CrossRef] [PubMed]
245. Ren, A.; Zou, J.; Lai, H.; Huang, Y.; Yuan, L.; Xu, H.; Shen, K.; Wang, H.; Wei, S.; Wang, Y.; et al. Direct Laser-Patterned MXene-Perovskite Image Sensor Arrays for Visible-Near Infrared Photodetection. *Mater. Horiz.* **2020**, *7*, 1901–1911. [CrossRef]
246. Yin, J.; Tan, Z.; Hong, H.; Wu, J.; Yuan, H.; Liu, Y.; Chen, C.; Tan, C.; Yao, F.; Li, T.; et al. Ultrafast and Highly Sensitive Infrared Photodetectors Based on Two-Dimensional Oxyselenide Crystals. *Nat. Commun.* **2018**, *9*, 3311. [CrossRef] [PubMed]
247. Feng, X.; He, Y.; Qu, W.; Song, J.; Pan, W.; Tan, M.; Yang, B.; Wei, H. Spray-Coated Perovskite Hemispherical Photodetector Featuring Narrow-Band and Wide-Angle Imaging. *Nat. Commun.* **2022**, *13*, 6106. [CrossRef] [PubMed]
248. Zhang, H.-S.; Dong, X.-M.; Zhang, Z.-C.; Zhang, Z.-P.; Ban, C.-Y.; Zhou, Z.; Song, C.; Yan, S.-Q.; Xin, Q.; Liu, J.-Q.; et al. Co-Assembled Perylene/Graphene Oxide Photosensitive Heterobilayer for Efficient Neuromorphics. *Nat. Commun.* **2022**, *13*, 4996. [CrossRef]
249. Lee, S.; Peng, R.; Wu, C.; Li, M. Programmable Black Phosphorus Image Sensor for Broadband Optoelectronic Edge Computing. *Nat. Commun.* **2022**, *13*, 1485. [CrossRef] [PubMed]
250. Kim, W.; Kim, H.; Yoo, T.J.; Lee, J.Y.; Jo, J.Y.; Lee, B.H.; Sasikala, A.A.; Jung, G.Y.; Pak, Y. Perovskite Multifunctional Logic Gates via Bipolar Photoresponse of Single Photodetector. *Nat. Commun.* **2022**, *13*, 720. [CrossRef]
251. Tang, Y.; Jin, P.; Wang, Y.; Li, D.; Chen, Y.; Ran, P.; Fan, W.; Liang, K.; Ren, H.; Xu, X.; et al. Enabling Low-Drift Flexible Perovskite Photodetectors by Electrical Modulation for Wearable Health Monitoring and Weak Light Imaging. *Nat. Commun.* **2023**, *14*, 4961. [CrossRef] [PubMed]
252. Jiang, B.-H.; Hsiao, F.-C.; Lin, Y.-R.; Lin, C.-H.; Shen, Y.A.; Hsu, Y.-Y.; Lee, P.-H.; Su, Y.-W.; Lu, H.-R.; Lin, C.-W.; et al. Highly Efficient Ternary Near-Infrared Organic Photodetectors for Biometric Monitoring. *ACS Appl. Mater. Interfaces* **2023**, *15*, 10907–10917. [CrossRef]
253. Simões, J.; Dong, T.; Yang, Z. Non-Fullerene Acceptor Organic Photodetector for Skin-Conformable Photoplethysmography Applications. *Adv. Mater. Interfaces* **2022**, *9*, 2101897. [CrossRef]
254. Dai, M.; Wang, C.; Qiang, B.; Jin, Y.; Ye, M.; Wang, F.; Sun, F.; Zhang, X.; Luo, Y.; Wang, Q.J. Long-Wave Infrared Photothermoelectric Detectors with Ultrahigh Polarization Sensitivity. *Nat. Commun.* **2023**, *14*, 3421. [CrossRef] [PubMed]
255. Goldstein, J.; Lin, H.; Deckoff-Jones, S.; Hempel, M.; Lu, A.-Y.; Richardson, K.A.; Palacios, T.; Kong, J.; Hu, J.; Englund, D. Waveguide-Integrated Mid-Infrared Photodetection Using Graphene on a Scalable Chalcogenide Glass Platform. *Nat. Commun.* **2022**, *13*, 3915. [CrossRef] [PubMed]

Disclaimer/Publisher's Note: The statements, opinions and data contained in all publications are solely those of the individual author(s) and contributor(s) and not of MDPI and/or the editor(s). MDPI and/or the editor(s) disclaim responsibility for any injury to people or property resulting from any ideas, methods, instructions or products referred to in the content.